

1
2
3
4
5
6
7
8
9
10
11
12
13
14
15
16
17
18
19
20
21
22
23
24
25
26
27
28
29
30
31
32
33
34
35
36
37
38
39
40
41
42
43
44

**Antecedent North Pacific Jet Regimes Conducive to the Development of
Continental U.S. Extreme Temperature Events during the Cool Season**

By

ANDREW C. WINTERS^{1*}, LANCE F. BOSART¹, and DANIEL KEYSER¹

¹Department of Atmospheric and Environmental Sciences
University at Albany, State University of New York
Albany, NY 12222

Submitted for publication in *Weather and Forecasting*
27 September 2018

* *Corresponding author address:* Andrew C. Winters, Dept. of Atmospheric and Environmental Sciences, University at Albany, SUNY, 1400 Washington Ave., Albany, NY 12222. E-mail: acwinters@albany.edu

45 ABSTRACT

46
47 This study considers the development of continental U.S. extreme temperature events
48 (ETEs) during the cool season (Sep–May), where extreme temperatures are defined in terms of
49 percentiles and events are defined in terms of the spatial coverage of extreme temperatures.
50 Following their identification, ETEs are classified into geographic clusters and stratified based
51 on the state of the North Pacific jet (NPJ) stream prior to ETE initiation using an NPJ Phase
52 Diagram. The NPJ Phase Diagram is developed from the two leading modes of NPJ variability
53 during the cool season. The first mode corresponds to a zonal extension or retraction of the exit
54 region of the climatological NPJ, while the second mode corresponds to a poleward or
55 equatorward shift of the exit region of the climatological NPJ.

56 The projection of 250-hPa zonal wind anomalies onto the NPJ Phase Diagram prior to
57 ETEs demonstrates that the preferred state and evolution of the NPJ prior to ETEs varies
58 considerably based on the geographic location of ETE initiation and the season. Southern Plains
59 extreme warm events are an exception, however, since extreme warm events in that location
60 most frequently initiate following a retracted NPJ during all seasons. The NPJ Phase Diagram is
61 subsequently utilized to examine a synoptic-scale flow evolution highly conducive to the
62 initiation of southern Plains extreme warm events via composite analysis. The composite
63 analysis demonstrates that a retracted NPJ supports an amplification of the upper-tropospheric
64 flow pattern over North America, which then induces persistent lower-tropospheric warm-air
65 advection over the southern Plains prior to ETE initiation.

66
67
68
69
70
71

72 **1. Introduction**

73 The occurrence of extreme temperature events (ETEs) during the cool season (Sep–May)
74 is often accompanied by considerable societal and economic impacts. Extreme cold events, in
75 particular, are responsible for about 30 deaths per year in the United States (NWS 2018), can
76 result in substantial damage to infrastructure (e.g., Cellitti et al. 2006), and can induce
77 agricultural and economic losses (e.g., Rogers and Rohli 1991; Gu et al. 2008; Dole et al. 2014;
78 Wolter et al. 2015). While extreme warm events during the cool season have received
79 comparatively less consideration within the refereed literature, they also pose considerable risks.
80 These risks include the development of floods and ice jams on waterways due to rapid snow and
81 ice melt (e.g., Westby et al. 2013), economic losses for industries reliant upon wintry conditions
82 (e.g., Westby et al. 2013), and the potential loss of early season agricultural products when an
83 extreme warm event is followed by a hard freeze (e.g., Rogers and Rohli 1991; Gu et al. 2008;
84 Westby et al. 2013; Dole et al. 2014; Peterson and Abatzoglou 2014; Westby and Black 2015).

85 From a climatological perspective, the development of one or several ETEs during a
86 single season can contribute disproportionately to temperature anomaly statistics for that
87 particular season (e.g., Hoerling et al. 2013; Peterson et al. 2013; Dole et al. 2014; Hartmann
88 2015; Wolter et al. 2015). The disproportionate contribution of ETEs to seasonal temperature
89 anomaly statistics suggests that ETEs need to be considered in order to understand the dynamical
90 and thermodynamic processes that operate at the weather–climate intersection. Such
91 investigations of ETEs are of additional importance given projected changes in the frequency of
92 ETEs within future climates (e.g., Walsh et al. 2001; Meehl and Tebaldi 2004; Portis et al. 2006;
93 Vavrus et al. 2006; Peterson et al. 2013; Westby et al. 2013; Scherer and Diffenbaugh 2014;
94 Grotjahn et al. 2016).

95 Numerous studies have sought relationships between cool season ETEs over North
96 America and modes of intraannual climate variability as part of an effort to understand the large-
97 scale meteorological patterns associated with the development of ETEs (Table 1). For example,
98 prior work has identified relationships between ETEs and the phase of the Pacific–North
99 American pattern (PNA), the North Atlantic Oscillation (NAO), the Arctic Oscillation (AO), and
100 the Madden–Julian Oscillation (MJO). Cool season ETEs have also been related to modes of
101 interannual climate variability such as the phase of the Pacific Decadal Oscillation (PDO) and
102 the El Niño–Southern Oscillation (ENSO). Subseasonal and seasonal forecasts of ETEs, in
103 particular, benefit considerably from knowledge of these relationships.

104 In addition to intraannual and interannual modes of climate variability, Loikith and
105 Broccoli (2014) emphasize that the synoptic-scale flow pattern plays an important role in the
106 development of ETEs, especially during the boreal winter. In particular, regional case studies and
107 composite analyses of cool season ETEs over North America have identified attributes of the
108 synoptic-scale flow pattern that are often associated with the development of ETEs. Common
109 attributes among these studies include an amplified upper-tropospheric flow pattern over North
110 America (e.g., Dallavalle and Bosart 1975; Hartjenstein and Bleck 1991; Colle and Mass 1995;
111 Konrad 1996; Cellitti et al. 2006; Loikith and Broccoli 2012; Westby and Black 2015; Xie et al.
112 2017), the development of surface cyclones and anticyclones that facilitate the transport of
113 anomalous cold or warm air into a region (e.g., Dallavalle and Bosart 1975; Colucci and
114 Davenport 1987; Konrad and Colucci 1989; Colle and Mass 1995; Konrad 1996; Walsh et al.
115 2001; Westby and Black 2015; Grotjahn and Zhang 2017; Xie et al. 2017), and topographical
116 processes such as cold-air damming (e.g., Bell and Bosart 1988; Hartjenstein and Bleck 1991;
117 Colle and Mass 1995) and the adiabatic warming of air parcels induced by lee subsidence (e.g.,

118 Brewer et al. 2012, 2013). Thermodynamic factors such as antecedent precipitation and soil
119 moisture (e.g., Turner and Gyakum 2011; Brewer et al. 2013; Hoerling et al. 2013; Dole et al.
120 2014), as well as adiabatic and diabatic processes occurring along air parcel trajectories in the
121 absence of topography (e.g., Konrad and Colucci 1989; Walsh et al. 2001; Portis et al, 2006;
122 Turner and Gyakum 2011) can also contribute to the development of ETEs.

123 While the synoptic-scale flow patterns associated with cool season ETEs feature common
124 attributes, it is apparent that the structure and evolution of these flow patterns are highly
125 dependent on the geographic location of the ETE and the meteorological season (e.g., Loikith
126 and Broccoli 2012, 2014; Westby et al. 2013; Westby and Black 2015; Grotjahn et al. 2016;
127 Grotjahn and Zhang 2017; Loikith et al. 2017; Xie et al. 2017). On the basis of these
128 relationships, Grotjahn et al. (2016) recommend in their review of large-scale meteorological
129 patterns associated with ETEs that additional work be conducted (1) to determine whether more
130 than one type of large-scale meteorological flow pattern is conducive to the development of
131 ETEs in a particular geographic location, and (2) to increase understanding of the synoptic-
132 dynamic mechanisms that support the development of large-scale meteorological flow patterns
133 associated with ETEs. These two recommendations motivate the present study.

134 Case studies of extreme weather events (EWEs) over North America demonstrate that the
135 state and evolution of the North Pacific jet (NPJ) stream can support the establishment of a
136 downstream environment that is conducive to EWEs (e.g., Cordeira and Bosart 2010; Bosart et
137 al. 2017). Consequently, the present study addresses the two recommendations from Grotjahn et
138 al. (2016) by adopting an objective NPJ-centered framework to determine the configurations of
139 the NPJ, or NPJ regimes, that are conducive to the development of continental U.S. ETEs during
140 the cool season. The adoption of this framework permits an examination of the degree to which

141 the preferred NPJ configurations prior to ETEs differ depending on both the geographic location
142 of the ETE within the continental U.S. and the meteorological season.

143 The remainder of this manuscript is structured as follows. Section 2 introduces an
144 identification scheme for continental U.S. ETEs as well as an NPJ Phase Diagram that will be
145 used to characterize the state and evolution of the NPJ prior to the development of ETEs during
146 the cool season. Section 3 discusses the characteristics of the NPJ prior to the development of
147 continental U.S. ETEs during the cool season employing the NPJ Phase Diagram. Section 4
148 provides an illustrative example demonstrating how the NPJ Phase Diagram can be utilized to
149 examine a synoptic-scale flow evolution that is highly conducive to the development of southern
150 Plains extreme warm events. Section 5 offers a discussion of the results from previous sections
151 and the implications those results may have for operational forecasts of ETEs.

152 **2. Methodology**

153 *a) ETE identification scheme*

154 Given that analyses of 2-m temperature are not available from the National Centers for
155 Environmental Prediction Climate Forecast System Reanalysis (CFSR; Saha et al. 2010, 2014),
156 this study utilizes 1-h forecasts of 2-m temperature from the CFSR during the 36-year period,
157 1979–2014. The 1-h forecasts of 2-m temperature from the CFSR are 0.5°-resolution, are
158 initialized every 6 h at the standard analysis times (i.e., 0000, 0600, 1200, and 1800 UTC), and
159 represent a uniformly gridded and temporally continuous dataset of 2-m temperatures that is
160 suitable for identifying continental U.S. ETEs during the period of study. The discussion that
161 follows outlines the ETE identification scheme with respect to continental U.S. extreme warm
162 events. Adaptations to the ETE identification scheme are then described in order to identify
163 continental U.S. extreme cold events.

164 To identify extreme warm events, 2-m temperature distributions are constructed for each
165 grid point at every forecast verification time during the year (i.e., 4 times daily at 0100, 0700,
166 1300, and 1900 UTC). A 2-m temperature distribution is constructed for a grid point at a single
167 verification time by isolating the 2-m temperatures for that grid point at 24-h intervals within a
168 21-day window centered on the verification time for every year between 1979 and 2014. A
169 sample 2-m temperature distribution for the 21-day window centered on 1900 UTC 30 May
170 during 1979–2014 is provided in Fig. 1a for a grid point near Albany, NY.

171 The 2-m temperature distributions are then utilized to objectively define thresholds for
172 extreme warmth that are specific to each grid point at a particular verification time. Extreme
173 warm temperatures are defined in the present study as those temperatures that are greater than
174 the 99th-percentile temperature for a grid point at a particular verification time. For the 2-m
175 temperature distribution constructed for a grid point near Albany, NY, the 99th-percentile
176 temperature is 32°C (90°F) at 1900 UTC 30 May (Fig. 1a). A horizontal distribution of the 99th-
177 percentile temperature at 1900 UTC 30 May highlights the effects of orography and bodies of
178 water on the magnitude of the 99th-percentile temperature (Fig. 1b).

179 To ensure that the ETE identification scheme captures areas of extreme warmth that are
180 concentrated within the same geographic region, the continental U.S. is split into two domains to
181 the east and west of 105°W¹, respectively (Fig. 1b). For each domain, 1-h forecasts of 2-m
182 temperature that exhibit at least one grid point over land with a temperature greater than its
183 respective 99th-percentile temperature are catalogued. The catalogued 1-h forecasts within each
184 domain are subsequently ranked according to the number of grid points with temperatures
185 greater than their respective 99th-percentile temperatures. Those 1-h forecasts that rank in the top

¹ 105°W is chosen given that it parallels the easternmost extent of the Rocky Mountains, which serve as a natural geographic barrier suitable for partitioning the continental U.S.

186 5% in terms of the number of grid points exhibiting extreme warmth are isolated and labeled as
187 extreme warm events within that spatial domain. For example, at least 224 grid points must
188 exhibit temperatures greater than their respective 99th-percentile temperatures in order for a
189 particular 1-h forecast to qualify as an extreme warm event within the eastern U.S. domain (Fig.
190 1c). By imposing a minimum gridpoint threshold, the identification scheme ensures that ETEs
191 are extreme not only with respect to temperature but also the spatial extent of extreme
192 temperature.

193 Lastly, extreme warm events that occurred within 24 h of another extreme warm event
194 are considered to be the same event, and all events are subsequently classified based on the
195 meteorological season [i.e., fall (Sep–Nov), winter (Dec–Feb), spring (Mar–May), summer (Jun–
196 Aug)] at the time of event initiation. The identification scheme for extreme warm events yields
197 304 and 264 extreme warm events during 1979–2014 within the eastern and western U.S.
198 domains, respectively (Table 2). An analogous scheme is employed to identify continental U.S.
199 extreme cold events by cataloguing 1-h forecasts of 2-m temperature with grid points that exhibit
200 temperatures less than their respective 1st-percentile temperatures. The identification scheme
201 yields 225 and 269 extreme cold events during 1979–2014 within the eastern and western U.S.
202 domains, respectively (Table 2). The identified ETEs are subsequently filtered to retain only cool
203 season ETEs (Table 2) for the forthcoming analysis in sections 3 and 4.

204 Frequency distributions indicating where extreme warm events initiate within the eastern
205 and western U.S. domains during the cool season are shown in Figs. 2a,b, respectively, along
206 with the individual event centroids of every extreme warm event at the time of event initiation.
207 The centroid for an individual extreme warm event at the time of event initiation is determined
208 by calculating a weighted average of the latitude and longitude of every grid point that exhibited

209 a temperature greater than its respective 99th-percentile temperature. In calculating the weighted
210 average, the latitude and longitude at every qualifying grid point is multiplied by the magnitude
211 of the difference between the temperature at the grid point and the 99th-percentile temperature
212 for the grid point. Consequently, an event centroid is focused on those grid points where
213 temperatures exceed their respective 99th-percentile temperatures by the largest magnitudes.

214 A frequency maximum in eastern U.S. extreme warm event initiation is observed in the
215 northern Plains, with a secondary maximum extending from the central and southern Plains
216 eastward towards the southern Mississippi River valley (Fig. 2a). Extreme warm events that
217 impact the U.S. East Coast during their lifespan often initiate upstream over the central U.S.
218 before progressing eastward, which may contribute to the lower frequency of extreme warm
219 event initiation observed near the U.S. East Coast compared to locations farther upstream. In
220 order to investigate whether the NPJ regimes that most frequently precede extreme warm event
221 initiation differ based on the location of event initiation, *k*-means clustering is used to classify the
222 eastern U.S. extreme warm event centroids into three geographic clusters: the “Northern Plains,”
223 “Southern Plains,” and “East Coast”. The event centroids shown in Fig. 2a are colored based on
224 their respective geographic cluster and match favorably with those locations that exhibit relative
225 maxima in extreme warm event initiation. The frequency distribution for western U.S. extreme
226 warm event initiation features two primary maxima located in the Pacific Northwest and in the
227 northern U.S. Rocky Mountains, respectively, and a secondary maximum in the southwestern
228 U.S. (Fig. 2b). As for eastern U.S. extreme warm events, *k*-means clustering is used to classify
229 the western U.S. extreme warm event centroids into three geographic clusters: the “Pacific
230 Northwest,” “Northern Rockies,” and “Southwest”.

231 Frequency distributions indicating where extreme cold events initiate within the eastern

232 and western U.S. domains during the cool season are shown in Figs. 3a,b, respectively. Eastern
233 U.S. extreme cold events most frequently initiate in the northern and southern Plains, with
234 relative maxima also observed in the northeastern Great Lakes region and the middle Mississippi
235 River valley (Fig. 3a). In contrast to eastern U.S. extreme warm events, four geographic clusters
236 are required in order to classify the extreme cold event centroids in a manner consistent with
237 those locations that experience the highest frequency of extreme cold event initiation: the
238 “Northern Plains,” “Northeast,” “Southern Plains,” and “Southeast”. For western U.S. extreme
239 cold event initiation, a frequency maximum is observed in the northern U.S. Rocky Mountains,
240 with a secondary maximum extending along the U.S. West Coast and into the southwestern U.S.
241 (Fig. 3b). As for western U.S. extreme warm events, the western U.S. extreme cold event
242 centroids are classified into three geographic clusters: the “Pacific Northwest,” “Northern
243 Rockies,” and “Southwest”.

244 *b) The NPJ Phase Diagram*

245 The NPJ regimes that precede continental U.S. ETEs are determined using an NPJ Phase
246 Diagram that is developed from the two leading modes of 250-hPa zonal wind variability over
247 the North Pacific during the cool season. The discussion in this subsection is adapted from
248 Winters et al. (2018) and is presented here given its relevance to the current study. The NPJ
249 Phase Diagram is developed utilizing 250-hPa zonal wind anomalies from the CFSR at every 6-h
250 analysis time during 1979–2014 excluding the summer months (Jun–Aug). Anomalies are
251 calculated as the deviation of the instantaneous 250-hPa zonal wind from a 21-day running mean
252 centered on each analysis time in order to remove the 36-year mean as well as the annual and
253 diurnal cycles. The 21-day running mean at a particular analysis time is calculated from 250-hPa
254 zonal wind data taken at 24-h intervals within a 21-day window centered on the analysis time for

255 every year between 1979 and 2014. A traditional empirical orthogonal function (EOF) analysis
256 (Wilks 2011, chapter 12) is subsequently performed on the 250-hPa zonal wind anomaly data
257 within a horizontal domain bounded in latitude from 10°N to 80°N and in longitude from 100°E
258 to 120°W in order to encompass the upper-tropospheric flow pattern over the North Pacific basin
259 and to determine the two leading modes of NPJ variability.

260 The regression of 250-hPa zonal wind anomaly data onto the first two standardized
261 principal components, PC 1 and PC 2, obtained from the traditional EOF analysis reveals the
262 spatial structures of EOF 1 and EOF 2 (Figs. 4a,b, respectively). EOF 1 explains 10.3% of the
263 variance of the 250-hPa zonal wind over the North Pacific during the cool season and
264 corresponds to longitudinal variability of the 250-hPa zonal wind in the vicinity of the exit
265 region of the climatological NPJ. A positive EOF 1 pattern is associated with a zonal extension
266 of the exit region of the climatological NPJ (i.e., a jet extension), while a negative EOF 1 pattern
267 is associated with a retraction of the exit region of the climatological NPJ (i.e., a jet retraction).
268 EOF 2 explains 7.8% of the variance of the 250-hPa zonal wind over the North Pacific during the
269 cool season and corresponds to latitudinal variability of the 250-hPa zonal wind in the vicinity of
270 the exit region of the climatological NPJ. A positive EOF 2 pattern is associated with a poleward
271 shift of the exit region of the climatological NPJ (i.e., a poleward shift), while a negative EOF 2
272 pattern is associated with an equatorward shift of the exit region of the climatological NPJ (i.e.,
273 an equatorward shift).

274 The EOF patterns and the combined variance explained by EOF 1 and EOF 2 are
275 comparable to those found in previous studies of NPJ variability (Athanasiadis et al. 2010; Jaffe
276 et al. 2011; Griffin and Martin 2017) and the two leading EOFs are statistically well separated
277 using the methodology outlined in North et al. (1982). Furthermore, the combined variance

278 explained by EOF 1 and EOF 2 is comparable to the variance explained by well-established
279 atmospheric teleconnection patterns, such as in Wheeler and Hendon (2004) for the MJO,
280 Barnston and Livesey (1987) for the PNA and the NAO, and Thompson and Wallace (1998) for
281 the AO.

282 The magnitudes and signs of PC 1 and PC 2 are normalized to unit variance and time
283 series constructed from the instantaneous PCs assist in characterizing the temporal evolution of
284 the NPJ with respect to EOF 1 and EOF 2. The use of instantaneous PCs produces a noisy time
285 series, however, due to the high-frequency variability that characterizes the NPJ on daily time
286 scales (e.g., Griffin and Martin 2017; their Fig. 1). Consequently, the instantaneous PCs are
287 smoothed through the calculation of a weighted average of the instantaneous PCs within ± 24 h of
288 each analysis time, t_0 . The weight, w , applied to the instantaneous PCs at each analysis time, t ,
289 within ± 24 h of t_0 is defined as: $w = 5 - |t - t_0|/6$, for $|t - t_0| \leq 24$ h.

290 The weighted PCs at a particular analysis time can be plotted on a two-dimensional
291 Cartesian grid (i.e., the NPJ Phase Diagram) in an effort to visualize the state of the NPJ and to
292 define the prevailing NPJ regime (Fig. 5). The position along the abscissa (ordinate) within the
293 NPJ Phase Diagram corresponds to the value of weighted PC 1 (weighted PC 2) and indicates
294 how strongly the 250-hPa zonal wind anomalies project onto EOF 1 (EOF 2). It is important to
295 note that the upper-tropospheric flow pattern over the North Pacific at any particular time is
296 more complex than that suggested by the NPJ Phase Diagram. Nevertheless, given that the NPJ
297 Phase Diagram is constructed from the two leading modes of 250-hPa zonal wind variability
298 over the North Pacific, plotting the weighted PCs in the NPJ Phase Diagram and tracking their
299 evolution over time encompasses many important aspects of the NPJ evolution.

300 As demonstrated extensively in prior work (e.g., Athanasiadis et al. 2010; Jaffe et al.

301 2011; Griffin and Martin 2017; Winters et al. 2018), each NPJ regime exhibits a strong influence
302 on the character of the downstream large-scale flow pattern over North America. To illustrate
303 this influence, the weighted PCs are calculated for all analysis times in the CFSR during 1979–
304 2014 excluding the summer months and are subsequently classified into NPJ regimes according
305 to Fig. 5. As in Winters et al. (2018), periods during which the NPJ is a Euclidean distance of at
306 least 1 standard deviation from the origin of the NPJ Phase Diagram and characterized by the
307 same NPJ regime for at least three consecutive days are isolated for composite analysis.
308 Composite analyses of the upper- (Fig. 6) and lower- (Fig. 7) tropospheric flow patterns 4 days
309 following the initiation of each NPJ regime describe the characteristic structure of the NPJ
310 associated with each NPJ regime, as well as the relationship between each NPJ regime and
311 lower-tropospheric temperatures over North America.

312 A jet extension features a strong, zonally oriented NPJ that extends towards the U.S.
313 West Coast (Fig. 6a) and is associated with above- and below-normal temperatures over western
314 and eastern North America, respectively (Fig. 7a). A jet retraction is characterized by an
315 anomalous upper-tropospheric ridge over the central North Pacific that is associated with a
316 retracted NPJ over the western North Pacific and a split NPJ to the east of the dateline (Fig. 6b).
317 Jet retractions are associated with below-normal temperatures along the west coast of North
318 America and above-normal temperatures in parts of the southern Plains and Ohio River valley
319 (Fig. 7b). A poleward shift is characterized by a strong NPJ whose exit region is deflected
320 poleward towards the Pacific Northwest (Fig. 6c), as well as above-normal temperatures across
321 northern North America (Fig. 7c). Lastly, an equatorward shift is associated with an anomalous
322 upper-tropospheric ridge over the high-latitude North Pacific and an anomalous trough over the
323 subtropical North Pacific, reminiscent of a Rex block (Rex 1950), that results in an equatorward

324 deflection of the NPJ (Fig. 6d). Below-normal temperatures are observed across northern North
325 America in conjunction with an equatorward shift (Fig. 7d).

326 Considered together, the composite analyses suggest that certain parts of North America
327 may be more susceptible than others to the development of an ETE based on the prevailing NPJ
328 regime. To evaluate the validity of this suggestion, the prevailing NPJ regime prior to each
329 continental U.S. ETE is determined by calculating the weighted PCs at 6-h intervals during the
330 3–7-day period prior to ETE initiation. The weighted PCs are then averaged to determine the
331 mean position of the NPJ within the NPJ Phase Diagram 3–7 days prior ETE initiation. Lastly,
332 every ETE is classified into an NPJ regime based on the mean position of the NPJ within the NPJ
333 Phase Diagram prior to ETE initiation according to Fig. 5. This classification of ETEs based on
334 the prevailing NPJ regime prior to ETE initiation is utilized in section 3 to determine the NPJ
335 regimes and evolutions that are preferred prior to the development of ETEs.

336 **3. NPJ regimes and evolutions that precede cool season ETEs**

337 *a) Extreme warm events*

338 The frequency with which eastern U.S. extreme warm events initiate following each NPJ
339 regime and during each meteorological season is shown in Fig. 8. Overall, eastern U.S. (Fig. 8a)
340 extreme warm events most frequently initiate following jet retractions (N=69) and poleward
341 shifts (N=66) during the cool season. Both jet retractions and poleward shifts are often associated
342 with the presence of upper-tropospheric ridges (Figs. 6b,c) and above-normal lower-tropospheric
343 temperatures (Figs. 7b,c) over parts of eastern North America. Consequently, jet retractions and
344 poleward shifts exhibit large-scale flow patterns that are generally more conducive to the
345 development of anomalous warmth over the eastern U.S. (Figs. 7b,c) than jet extensions and
346 equatorward shifts (Figs. 7a,d). The preferred NPJ regime prior to eastern U.S. extreme warm

347 event initiation during the cool season varies, however, based on the geographic location of event
348 initiation. In particular, both Northern Plains (Fig. 8b) and East Coast (Fig. 8d) extreme warm
349 events most frequently initiate following poleward shifts (N=28 and N=20, respectively) during
350 the cool season, while Southern Plains (Fig. 8c) events most frequently initiate following jet
351 retractions (N=35) by a large margin compared to the other NPJ regimes.

352 The most frequent NPJ regime prior to eastern U.S. extreme warm event initiation also
353 varies seasonally, with the exception of Southern Plains events. Specifically, eastern U.S. (Fig.
354 8a) extreme warm events most frequently initiate following equatorward shifts (N=26) during the
355 fall, following jet retractions (N=27) during the winter, and following both jet retractions (N=20)
356 and poleward shifts (N=20) during the spring. While Northern Plains (Fig. 8b) and East Coast
357 (Fig. 8d) extreme warm events also exhibit seasonal variability with respect to the preferred NPJ
358 regime prior to event initiation, Southern Plains (Fig. 8c) events most frequently initiate
359 following jet retractions during all seasons.

360 The frequency with which western U.S. extreme warm events initiate following each NPJ
361 regime and during each meteorological season is shown in Fig. 9. Western U.S. (Fig. 9a) extreme
362 warm events initiate more frequently following poleward shifts (N=56), equatorward shifts
363 (N=54), and jet extensions (N=53) compared to jet retractions (N=41) during the cool season.
364 The relatively low frequency of jet retractions prior to western U.S. extreme warm event
365 initiation is consistent with the observation that jet retractions are the only NPJ regime associated
366 with an anomalous upper-tropospheric trough (Fig. 6b) and below-normal lower-tropospheric
367 temperatures (Fig. 7b) along the U.S. West Coast. Consequently, jet retractions are often
368 associated with a large-scale flow pattern over the western U.S. that is generally less conducive
369 to the development of anomalous warmth than the other NPJ regimes.

370 As observed for eastern U.S. extreme warm events, the most frequent NPJ regimes prior
371 to western U.S. extreme warm event initiation during the cool season vary among the western
372 U.S. geographic clusters. In particular, Pacific Northwest (Fig. 9b) extreme warm events most
373 frequently initiate following jet extensions (N=27) and equatorward shifts (N=27) during the
374 cool season, while Southwest (Fig. 9d) events most frequently initiate following equatorward
375 shifts (N=20) and poleward shifts (N=19). Northern Rockies (Fig. 9c) extreme warm events
376 initiate following poleward shifts (N=15) with the highest frequency during the cool season and,
377 unlike Pacific Northwest and Southwest events, initiate following equatorward shifts (N=7) with
378 the lowest frequency. The most frequent NPJ regimes prior to extreme warm event initiation also
379 tend to vary based on the meteorological season for all western U.S. extreme warm events (Fig.
380 9a) and for those events within each western U.S. geographic cluster (Figs. 9b–d). For example,
381 western U.S. extreme warm events (Fig. 9a) most frequently initiate following poleward shifts
382 (N=23) and jet retractions (N=19) during the fall, following jet extensions (N=32) and
383 equatorward shifts (N=25) during the winter, and following equatorward shifts (N=20) and
384 poleward shifts (N=18) during the spring.

385 The construction of composite trajectories of the NPJ within the NPJ Phase Diagram
386 provides an objective characterization of the evolution of the NPJ during the 10-day period prior
387 to extreme warm event initiation and indicates how the NPJ evolution may differ based on the
388 geographic location of an extreme warm event. Composite trajectories of the NPJ within the NPJ
389 Phase Diagram are constructed by calculating the weighted PCs at 6-h intervals during the 10-
390 day period prior to the initiation of each extreme warm event. The weighted PCs prior to each
391 extreme warm event are then shifted so that the position of the NPJ always lies at the origin of
392 the NPJ Phase Diagram 10 days prior to event initiation. This shift permits a comparison of the

393 NPJ evolution prior to extreme warm event initiation between the geographic clusters. Lastly, the
394 weighted PCs that correspond to the same lead time prior to extreme warm event initiation are
395 averaged across events within the same geographic cluster to construct a composite trajectory of
396 the NPJ within the NPJ Phase Diagram.

397 The composite trajectories of the NPJ within the NPJ Phase Diagram prior to all eastern
398 U.S. extreme warm events and prior to events within each eastern U.S. geographic cluster are
399 provided in Fig. 10a. Consistent with the observation that eastern U.S. extreme warm events
400 most frequently initiate following jet retractions and poleward shifts during the cool season (Fig.
401 8a), the composite trajectory for all eastern U.S. extreme warm events indicates that the NPJ
402 undergoes a retraction and poleward shift during the 10-day period prior to event initiation. A
403 comparable trajectory is generally observed for extreme warm events within each eastern U.S.
404 geographic cluster, with Northern Plains events characterized by an NPJ that undergoes a
405 poleward shift, and Southern Plains and East Coast events characterized by an NPJ that
406 undergoes a retraction.

407 The composite trajectory prior to all western U.S. (Fig. 10b) extreme warm events differs
408 considerably from the trajectory prior to all eastern U.S. (Fig. 10a) events. In particular, the
409 composite trajectory for all western U.S. extreme warm events indicates that the NPJ undergoes
410 an extension and equatorward shift during the 10-day period prior to event initiation, rather than
411 the retraction and poleward shift observed for all eastern U.S. events. The extension of the NPJ
412 prior to all western U.S. extreme warm events is consistent with the observation that western
413 U.S. events initiate following jet retractions with the lowest frequency during the cool season
414 (Fig. 9a). Considered together, the trajectories shown in Figs. 10a,b demonstrate that knowledge
415 of the evolution of the NPJ in the context of the NPJ Phase Diagram differentiates between NPJ

416 evolutions that are generally more conducive to the development of extreme warm events in the
417 eastern and western U.S.

418 In contrast to the eastern U.S. geographic clusters, the trajectories associated with the
419 western U.S. geographic clusters (Fig. 10b) differ notably from one another. Specifically, Pacific
420 Northwest extreme warm events are characterized by an NPJ that undergoes an extension,
421 Southwest events are characterized by an NPJ that undergoes an equatorward shift and retraction,
422 and Northern Rockies events are characterized by an NPJ that does not deviate far from the
423 origin of the NPJ Phase Diagram during the 10-day period prior to event initiation. The
424 trajectory for the Northern Rockies extreme warm events thus indicates that these events do not
425 appear to have a preferred NPJ evolution prior to event initiation.

426 *b) Extreme cold events*

427 The frequency with which eastern U.S. extreme cold events initiate following each NPJ
428 regime and during each meteorological season is shown in Fig. 11. Overall, eastern U.S. extreme
429 cold events (Fig. 11a) most frequently initiate following equatorward shifts (N=73) by a large
430 margin compared to the other NPJ regimes during the cool season. Equatorward shifts are often
431 associated with an anomalous upper-tropospheric trough (Fig. 6d) and below-normal lower-
432 tropospheric temperatures (Fig. 7d) across northern North America to the east of the Rocky
433 Mountains. Consequently, an equatorward shift is particularly conducive to the development of
434 anomalous cold across the eastern U.S. in the event that the large-scale flow pattern can facilitate
435 the equatorward transport of anomalously cold air from northern North America.

436 An examination of Figs. 11b–e further demonstrates that extreme cold events most
437 frequently initiate following equatorward shifts during the cool season for each eastern U.S.
438 geographic cluster. The similarity between geographic clusters with respect to the most frequent

439 NPJ regime prior to extreme cold event initiation stands in contrast to the differences observed
440 between geographic clusters with respect to the most frequent NPJ regime prior to eastern U.S.
441 extreme warm event initiation (Figs. 8b–d). This contrast between the geographic clusters
442 associated with eastern U.S. extreme cold events and warm events suggests that the upper-
443 tropospheric flow patterns over the North Pacific prior to eastern U.S. extreme cold events are
444 generally characterized by a lesser degree of variability than those prior to eastern U.S. extreme
445 warm events.

446 The most frequent NPJ regime prior to eastern U.S. extreme cold events (Fig. 11a) varies
447 as a function of meteorological season. In particular, eastern U.S. extreme cold events most
448 frequently initiate following both jet extensions (N=17) and equatorward shifts (N=17) during
449 the fall, and following only equatorward shifts during the winter (N=30) and spring (N=26). The
450 Northern Plains (Fig. 11b), Northeast (Fig. 11c), and Southeast (Fig. 11e) clusters also exhibit
451 seasonal variability with respect to the preferred NPJ regime prior to event initiation, while
452 events within the Southern Plains (Fig. 11d) cluster most frequently initiate following
453 equatorward shifts during all seasons.

454 The frequency with which western U.S. extreme cold events initiate following each NPJ
455 regime and during each meteorological season is shown in Fig. 12. Western U.S. extreme cold
456 events (Fig. 12a) most frequently initiate following jet retractions (N=59) during the cool season,
457 rather than with the lowest frequency (N=41) as observed for western U.S. extreme warm events
458 (Fig. 9a). Recall from section 3a that a jet retraction is the only NPJ regime associated with an
459 anomalous upper-tropospheric trough (Fig. 6b) and below-normal lower-tropospheric
460 temperatures (Fig. 7b) along the U.S. West Coast. Consequently, the large-scale flow pattern
461 associated with a jet retraction is generally more conducive to the development of western U.S.

462 extreme cold events than the other NPJ regimes. The most frequent NPJ regime prior to extreme
463 cold event initiation during the cool season differs, however, between the western U.S.
464 geographic clusters. In particular, Pacific Northwest (Fig. 12b) extreme cold events most
465 frequently initiate following jet retractions (N=31), Northern Rockies (Fig. 12c) events most
466 frequently initiate following equatorward shifts (N=22), and Southwest (Fig. 12d) events most
467 frequently initiate following jet extensions (N=19).

468 As for eastern U.S. extreme cold events (Fig. 11a), the most frequent NPJ regime prior to
469 western U.S. extreme cold event initiation (Fig. 12a) varies seasonally. In particular, western
470 U.S. extreme cold events most frequently initiate following equatorward shifts (N=21) and jet
471 extensions (N=18) during the fall, and following jet retractions during the winter (N=21) and
472 spring (N=28). While the most frequent NPJ regime prior to the initiation of Pacific Northwest
473 (Fig. 12b) and Southwest (Fig. 12d) events also varies seasonally, Northern Rockies (Fig. 12c)
474 events most frequently initiate following equatorward shifts during all seasons.

475 The composite trajectories of the NPJ within the NPJ Phase Diagram for all eastern (Fig.
476 13a) and all western (Fig. 13b) U.S. extreme cold events are comparable. Specifically, the
477 composite trajectories for all eastern and all western U.S. extreme cold events both indicate that
478 the NPJ undergoes an equatorward shift and slight extension during the 10-day period prior to
479 event initiation. Therefore, in contrast to continental U.S. extreme warm events (Figs. 10a,b),
480 knowledge of the evolution of the NPJ within the NPJ Phase Diagram alone does not
481 differentiate between NPJ evolutions that are generally more conducive to extreme cold event
482 initiation within the eastern and western U.S.

483 Subtle differences in the NPJ evolution prior to extreme cold event initiation are observed
484 between the geographic clusters. Similar to the trajectory for all eastern U.S. extreme cold

485 events, the composite trajectories prior to the initiation of Northern Plains, Southern Plains, and
486 Southeast events indicate that the NPJ primarily undergoes an equatorward shift during the 10-
487 day period prior to event initiation (Fig. 13a). The composite trajectory prior to the initiation of
488 Northeast extreme cold events differs from the other eastern U.S. clusters, however, with the NPJ
489 undergoing an extension rather than an equatorward shift during the 10-day period prior to event
490 initiation. The Pacific Northwest and Northern Rockies trajectories are comparable to the
491 trajectory for all western U.S. extreme cold events in that they both show the NPJ undergoing an
492 equatorward shift and slight extension by the time of event initiation (Fig. 13b). The Southwest
493 trajectory also indicates that the NPJ undergoes an equatorward shift but, unlike the Pacific
494 Northwest and Northern Rockies trajectories, the NPJ evolves towards a slight retraction, rather
495 than a slight extension, by the time of event initiation.

496 **4. Composite evolution of Southern Plains extreme warm events preceded by a jet** 497 **retraction**

498 The discussion in section 3 demonstrates that the most frequent NPJ regime and
499 evolution prior to continental U.S. ETEs during the cool season can vary considerably based on
500 the type of ETE and the geographic location of ETE initiation. Given these results, the NPJ
501 Phase Diagram can be utilized to isolate ETEs within a particular geographic location that
502 initiate following the same NPJ regime during the cool season. A composite analysis performed
503 on the isolated ETEs subsequently reveals the synoptic-dynamic mechanisms that allow the flow
504 to evolve from an antecedent NPJ regime to ETE initiation within a particular geographic region.
505 The forthcoming discussion provides an illustrative example that exposes the utility of such an
506 analysis by investigating the synoptic-scale flow evolution most conducive to Southern Plains
507 extreme warm events. The Southern Plains cluster is selected for analysis given that it is the only

508 geographic cluster in which the most frequent NPJ regime prior to extreme warm event initiation
509 does not vary seasonally (Fig. 8c). Furthermore, extreme warm events during the cool season are
510 selected due to the limited scrutiny warm events have received in the refereed literature
511 compared to cold events.

512 As discussed in section 3a, Southern Plains extreme warm events (Fig. 8c) most
513 frequently initiate following jet retractions (N=35) by a large margin compared to the other NPJ
514 regimes during the cool season. Consequently, a composite analysis of the synoptic-scale flow
515 evolution most conducive to Southern Plains extreme warm event initiation during the cool
516 season is performed by isolating only those Southern Plains extreme warm events that are
517 characterized by a jet retraction prior to event initiation. The latitude and longitude of the
518 individual Southern Plains event centroids (Fig. 2a) are then averaged to determine the position
519 of a composite centroid. The composite analyses are constructed, first, by shifting the CFSR data
520 for each event so that each individual event centroid matches the position of the composite
521 centroid and, second, by averaging the shifted CFSR data at each grid point within the horizontal
522 domain shown in Fig. 14 across all cases. A two-sided Student's t test is performed on composite
523 250-hPa geopotential height anomalies and 850-hPa temperature anomalies to identify regions
524 that are statistically distinct from climatology at the 99% confidence level.

525 The composite evolution of the synoptic-scale flow pattern during the 6-day period prior
526 to event initiation is provided in Fig. 14. An anomalous upper-tropospheric ridge is located over
527 the central North Pacific 6 days prior to event initiation, resulting in a retracted NPJ over the
528 western North Pacific and a split NPJ to the east of the dateline (Fig. 14a). Farther downstream,
529 an anomalous upper-tropospheric ridge is collocated with above-normal 850-hPa temperatures
530 over the southern Plains and northern Mexico (Fig. 14b), which suggests that the synoptic-scale

531 environment may be preconditioned for the development of extreme warmth in those locations.

532 Four days prior to event initiation, the anomalous North Pacific ridge amplifies compared
533 to the prior time in conjunction with surface cyclogenesis beneath the left-exit region of the
534 retracted NPJ (Figs. 14c,d). Specifically, the surface cyclone facilitates lower-tropospheric
535 warm-air advection over the central North Pacific that contributes to both upper-tropospheric
536 geopotential height rises and forcing for quasigeostrophic ascent (not shown). The occurrence of
537 implied ascent in the presence of positive precipitable water anomalies over the central North
538 Pacific suggests that latent heating is likely associated with any regions of ascent and,
539 consequently, that diabatic processes also contribute to the observed ridge amplification. The
540 role of diabatic processes during ridge amplification has been noted by a number of studies (e.g.,
541 Massacand et al. 2001; Riemer et al. 2008; Torn 2010; Grams et al. 2011; Madonna et al. 2014;
542 Pfahl et al. 2015; Torn and Hakim 2015; Grams and Archambault 2016; Bosart et al. 2017).

543 Central North Pacific ridge amplification subsequently results in the amplification of the
544 downstream upper-tropospheric flow pattern 2 days prior to event initiation (Fig. 14e), including
545 the development of a positively tilted upper-tropospheric trough along the west coast of North
546 America and additional ridge amplification over the southern Plains. The amplified upper-
547 tropospheric flow pattern supports lee cyclogenesis downstream of the northern U.S. Rocky
548 Mountains and surface anticyclogenesis over the southeast U.S. (Fig. 14f). The configuration of
549 the pressure gradient between the lee cyclone and surface anticyclone induces southwesterly
550 geostrophic flow over central North America and the concomitant advection of anomalous
551 warmth from northern Mexico towards the southern Plains.

552 At the time of event initiation, the lee cyclone intensifies compared to the prior time
553 beneath the entrance region of a 250-hPa jet streak and in conjunction with further amplification

554 of the upper-tropospheric flow pattern (Figs. 14g,h). The more intense lee cyclone subsequently
555 facilitates stronger southwesterly geostrophic flow over the southern Plains than at the prior time,
556 which ensures that the advection of anomalous warmth towards the southern Plains continues
557 unabated until the time of event initiation. The composite evolution also features large positive
558 precipitable water anomalies over the middle Mississippi River valley at the time of event
559 initiation compared to prior times (Fig. 14g). Given the strong dynamical forcing for ascent
560 provided by the amplified upper-tropospheric flow pattern and the presence of the lee cyclone,
561 the evolution of a Southern Plains extreme warm event strongly resembles synoptic-scale flow
562 evolutions that are conducive to eastern U.S. extreme precipitation events during the cool season
563 (e.g., Moore et al. 2015; Moore 2017). Consequently, it is hypothesized that extreme
564 precipitation events may often accompany Southern Plains extreme warm events.

565 **5. Discussion**

566 The utility of the NPJ Phase Diagram is that it provides a common framework for
567 characterizing the antecedent large-scale flow patterns associated with continental U.S. ETEs
568 during the cool season. Overall, eastern U.S. extreme warm events are most frequent following
569 jet retractions and poleward shifts and are characterized by an NPJ that evolves towards those
570 same two NPJ regimes within the NPJ Phase Diagram during the 10-day period prior to event
571 initiation. Western U.S. extreme warm events are the least frequent following jet retractions and
572 are characterized by an NPJ that evolves towards a jet extension and equatorward shift during the
573 10-day period prior to event initiation. Eastern U.S. extreme cold events are most frequent
574 following equatorward shifts compared to the other NPJ regimes by a large margin, while
575 western U.S. extreme cold events are most frequent following jet retractions. Furthermore, both
576 eastern and western U.S. extreme cold events are characterized by an NPJ that evolves towards

577 an equatorward shift and a slight jet extension during the 10-day period prior to event initiation.
578 The NPJ regimes that most frequently precede extreme warm and cold event initiation within
579 parts of the continental U.S. during the cool season are those that feature anomalously warm and
580 cold lower-tropospheric temperatures within the same parts of the continental U.S., respectively,
581 during a typical period characterized by those NPJ regimes (Fig. 7). Consequently, the results
582 from the present study suggest that knowledge of the prevailing NPJ regime and the subsequent
583 NPJ evolution provides an indication as to whether the large-scale flow pattern is more
584 conducive to the development of eastern and western U.S. ETEs compared to climatology.

585 While the NPJ regimes and evolutions described above are those that most frequently
586 precede all eastern and all western U.S. ETEs during the cool season, the most frequent NPJ
587 regime prior to ETE initiation varies considerably within the eastern and western U.S. domains
588 based on the specific geographic location of ETE initiation and the meteorological season. The
589 considerable geographic and seasonal variability that characterizes the most frequent NPJ regime
590 prior to ETE initiation is indicative of the variety of large-scale flow evolutions that are
591 conducive to ETE initiation within a specific geographic location. The NPJ Phase Diagram and
592 the results from the present study provide a foundation for detailed synoptic-dynamic
593 investigations into the variety of large-scale flow evolutions that facilitate ETE initiation within
594 specific geographic locations.

595 As an illustrative example, the NPJ Phase Diagram was utilized to examine the large-
596 scale flow evolution that is most conducive to the initiation of Southern Plains extreme warm
597 events during the cool season, given that extreme warm events in that location most frequently
598 initiate following jet retractions during all seasons. The composite analysis suggests that
599 Southern Plains extreme warm event initiation is dynamically driven within an environment that

600 is preconditioned for above-normal lower-tropospheric temperatures. Specifically, a retracted
601 NPJ supports an amplification of the upper-tropospheric flow pattern over North America, which
602 subsequently induces the transport of an anomalously warm lower-tropospheric air mass towards
603 the Southern Plains prior to event initiation.

604 The analysis performed for Southern Plains extreme warm events can be extended to
605 investigate the large-scale flow evolutions conducive to ETE initiation in other geographic
606 clusters. For instance, in geographic clusters where multiple NPJ regimes are frequently
607 observed prior to ETE initiation, such as for Pacific Northwest extreme cold events, the NPJ
608 Phase Diagram can be utilized to categorize ETEs based on the antecedent NPJ regime.
609 Composite analyses can then be performed on events that are preceded by the same NPJ regime
610 in order to examine the differences between a set of large-scale flow evolutions that are mutually
611 conducive to ETE initiation, and to identify the characteristic origins of anomalously warm and
612 cold air masses during the selected events. While not shown, it is hypothesized that subtle
613 differences in the location and character of upper-tropospheric flow amplification over the North
614 Pacific may explain the differences between geographic clusters regarding the preferred NPJ
615 regime and evolution prior to ETE initiation.

616 The capability of the NPJ Phase Diagram to identify NPJ regimes and evolutions that are
617 conducive to the development of ETEs suggests that the NPJ Phase Diagram may have utility
618 during the preparation of operational medium-range (6–10 day) temperature forecasts over the
619 continental U.S. In particular, the NPJ Phase Diagram can be employed operationally to
620 determine both the prevailing NPJ regime and the forecast evolution of the NPJ in real time.
621 Knowledge of the prevailing NPJ regime and evolution can then be paired with the results from
622 the present study to identify geographic locations that may be susceptible to the development of

623 anomalous lower-tropospheric temperatures during the medium-range period. Furthermore,
624 Winters et al. (2018) indicate that certain NPJ regimes are generally characterized by enhanced
625 or reduced medium-range forecast skill compared to climatology. Consequently, studies that
626 examine the medium-range forecast skill of large-scale environments prior to ETEs with respect
627 to the NPJ Phase Diagram may reveal whether certain large-scale flow evolutions prior to ETEs
628 exhibit enhanced or reduced forecast skill.

629 Lastly, the NPJ Phase Diagram can be utilized to examine the variability in NPJ regimes
630 that precede other types of North American EWEs during the cool season. As demonstrated for
631 ETEs, the application of the NPJ Phase Diagram can provide additional understanding of the
632 variety of large-scale environments that are conducive to extreme precipitation events (e.g.,
633 Moore et al. 2015; Moore 2017), landfalling atmospheric river events (e.g., Zhu and Newell
634 1998; Ralph et al. 2004; Neiman et al. 2008; Cordeira et al. 2013; Mundhenk et al. 2016;
635 Gershunov et al. 2017), severe weather outbreaks (e.g., Cook and Schaefer 2008; Allen et al.
636 2015; Tippett et al. 2015; Gensini and Marinaro 2016; Cook et al. 2017), and rapidly deepening
637 midlatitude cyclones (e.g., Sanders and Gyakum 1980; Bosart et al. 1996; Isard et al. 2000; Grise
638 et al. 2013; Bentley 2018). Results that emerge from these applications of the NPJ Phase
639 Diagram may translate into improved operational forecasts of EWEs.

640 *Acknowledgments*

641 The authors thank Mike Bodner, Daniel Halperin, Arlene Laing, Bill Lamberson, Sara Ganetis,
642 and Josh Kastman for their constructive discussions concerning the NPJ Phase Diagram. The
643 authors also thank the National Oceanic and Atmospheric Administration for its support of this
644 work via Grant NA15NWS4680006 and the National Science Foundation for its support of this
645 work via Grant AGS-1355960.

646 **References**

- 647
648 Allen, J. T., M. K. Tippett, and A. H. Sobel, 2015: Influence of the El Niño/Southern Oscillation
649 on tornado and hail frequency in the United States. *Nat. Geosci.*, **8**, 278–283, doi:
650 10.1038/ngeo2385.
- 651 Athanasiadis, P. J., J. M. Wallace, and J. J. Wettstein, 2010: Patterns of wintertime jet stream
652 variability and their relation to the storm tracks. *J. Atmos. Sci.*, **67**, 1361–1381, doi:
653 10.1175/2009JAS3270.1.
- 654 Barnston, A. G., and R. E. Livesey, 1987: Classification, seasonality, and persistence of low-
655 frequency atmospheric circulation patterns. *Mon. Wea. Rev.*, **115**, 1083–1126, doi:
656 10.1175/1520-0493(1987)115<1083:CSAPOL>2.0.CO;2.
- 657 Bell, G. D., and L. F. Bosart, 1988: Appalachian cold-air damming. *Mon. Wea. Rev.*, **116**, 137–
658 161, doi: 10.1175/1520-0493(1988)116<0137:ACAD>2.0.CO;2.
- 659 Bentley, A. M., 2018: Extratropical cyclones leading to extreme weather events over central and
660 eastern North America. Ph.D. Dissertation, University at Albany, SUNY, 158 pp.
- 661 Bosart, L. F., G. J. Hakim, K. R. Tyle, M. A. Bedrick, W. E. Bracken, M. J. Dickinson, and D.
662 M. Schultz, 1996: Large-scale antecedent conditions associated with the 12–14 March
663 1993 cyclone (“Superstorm ’93”) over eastern North America. *Mon. Wea. Rev.*, **124**,
664 1865–1891, doi: 10.1175/1520-0493(1996)124<1865:LSACAW>2.0.CO;2.
- 665 Bosart, L. F., B. J. Moore, J. M. Cordeira, and H. M. Archambault, 2017: Interactions of North
666 Pacific tropical, midlatitude, and polar disturbances resulting in linked extreme weather
667 events over North America in October 2007. *Mon. Wea. Rev.*, **145**, 1245–1273, doi:
668 10.1175/MWR-D-16-0230.1.

669 Brewer, M. C., C. F. Mass, and B. E. Potter, 2012: The west coast thermal trough: Climatology
670 and synoptic evolution. *Mon. Wea. Rev.*, **140**, 3820–3843, doi: 10.1175/MWR-D-12-
671 00078.1.

672 Brewer, M. C., C. F. Mass, and B. E. Potter, 2013: The west coast thermal trough: Mesoscale
673 evolution and sensitivity to terrain and surface fluxes. *Mon. Wea. Rev.*, **141**, 2869–2896,
674 doi: 10.1175/MWR-D-12-00305.1.

675 Carrera, M. L., R. W. Higgins, and V. E. Kousky, 2004: Downstream weather impacts associated
676 with atmospheric blocking over the northeast Pacific. *J. Climate*, **17**, 4823–4839, doi:
677 10.1175/JCLI-3237.1.

678 Cellitti, M. P., J. E. Walsh, R. M. Rauber, and D. H. Portis, 2016: Extreme cold air outbreaks
679 over the United States, the polar vortex, and the large-scale circulation. *J. Geophys. Res.*,
680 **111**, D02114, doi: 10.1029/2005JD006273.

681 Colle, B. A., and C. F. Mass, 1995: The structure and evolution of cold surges east of the Rocky
682 Mountains. *Mon. Wea. Rev.*, **123**, 2577–2610, doi: 10.1175/1520-
683 0493(1995)123<2577:TSAEOC>2.0.CO;2.

684 Colucci, S. J., and J. C. Davenport, 1987: Rapid surface anticyclogenesis: Synoptic climatology
685 and attendant large-scale circulation changes. *Mon. Wea. Rev.*, **115**, 822–836, doi:
686 10.1175/1520-0493(1987)115<0822:RSASCA>2.0.CO;2.

687 Cook, A. R., and J. T. Schaefer, 2008: The relation of El Niño–Southern Oscillation (ENSO) to
688 winter tornado outbreaks. *Mon. Wea. Rev.*, **136**, 3121–3137, doi:
689 10.1175/2007MWR2171.1.

690 Cook, A. R., L. M. Leslie, D. B. Parsons, and J. T. Schaefer, 2017: The impact of El Niño–
691 Southern Oscillation (ENSO) on winter and early spring U.S. tornado outbreaks. *J. Appl.*
692 *Meteor. Climatol.*, **56**, 2455–2478, doi: 10.1175/JAMC-D-16-0249.1.

693 Cordeira, J. M., and L. F. Bosart, 2010: The antecedent large-scale conditions of the “Perfect
694 Storms” of late October and early November 1991. *Mon. Wea. Rev.*, **138**, 2546–2569,
695 doi: 10.1175/2010MWR3280.1.

696 Cordeira, J. M., F. M. Ralph, and B. J. Moore, 2013: The development and evolution of two
697 atmospheric rivers in proximity to western North Pacific tropical cyclones in October
698 2010. *Mon. Wea. Rev.*, **141**, 4234–4255, doi: 10.1175/MWR-D-13-00019.1.

699 Dallavalle, J. P., and L. F. Bosart, 1975: A synoptic investigation of anticyclogenesis
700 accompanying North American polar air outbreaks. *Mon. Wea. Rev.*, **103**, 941–957, doi:
701 10.1175/1520-0493(1975)103<0941:ASIOAA>2.0.CO;2.

702 Dole, R., M. Hoerling, A. Kumar, J. Eischeid, J. Perlwitz, X.-W. Quan, G. Kiladis, R. Webb, D.
703 Murray, M. Chen, K. Wolter, and T. Zhang, 2014: The making of an extreme event:
704 Putting the pieces together. *Bull. Amer. Meteor. Soc.*, **95**, 427–440, doi: 10.1175/BAMS-
705 D-12-00069.1.

706 Downton, M. W., and K. A. Miller, 1993: The freeze risk to Florida citrus. Part II: Temperature
707 variability and circulation patterns. *J. Climate*, **6**, 364–372, doi: 10.1175/1520-
708 0442(1993)006<0364:TFRTFC>2.0.CO;2.

709 Gensini, V. A., and A. Marinaro, 2016: Tornado frequency in the United States related to global
710 relative angular momentum. *Mon. Wea. Rev.*, **144**, 801–810, doi: 10.1175/MWR-D-15-
711 0289.1.

712 Gershunov, A., T. Shulgina, F. M. Ralph, D. A. Lavers, and J. J. Rutz, 2017: Assessing the
713 climate-scale variability of atmospheric rivers affecting western North America.
714 *Geophys. Res. Lett.*, **44**, 7900–7908, doi: 10.1002/2017GL074175.

715 Grams, C. M., and Coauthors, 2011: The key role of diabatic processes in modifying the upper-
716 tropospheric wave guide: A North Atlantic case-study. *Quart. J. Roy. Meteor. Soc.*, **137**,
717 2174–2193, doi: 10.1002/qj.891.

718 Grams, C. M., and H. M. Archambault, 2016: The key role of diabatic outflow in amplifying the
719 midlatitude flow: A representative case study of weather systems surrounding western
720 North Pacific extratropical transition. *Mon. Wea. Rev.*, **144**, 3847–3869, doi:
721 10.1175/MWR-D-15-0419.1.

722 Griffin, K. S., and J. E. Martin, 2017: Synoptic features associated with temporally coherent
723 modes of variability of the North Pacific jet stream. *J. Climate*, **30**, 39–54, doi:
724 10.1175/JCLI-D-15-0833.1.

725 Grise, K. M., S.-W. Son, J. R. Gyakum, 2013: Intraseasonal and interannual variability in North
726 American storm tracks and its relationship to equatorial Pacific variability. *Mon. Wea.*
727 *Rev.*, **141**, 3610–3625, doi: 10.1175/MWR-D-12-00322.1.

728 Grotjahn, R., and Coauthors, 2016: North American extreme temperature events and related
729 large scale meteorological patterns: A review of statistical methods, dynamics, modeling,
730 and trends. *Climate Dyn.*, **46**, 1151–1184, doi: 10.1007/s00382-015-2638-6.

731 Grotjahn, R., and R. Zhang, 2017: Synoptic analysis of cold air outbreaks over the California
732 Central Valley. *J. Climate*, **30**, 9417–9433, doi: 10.1175/JCLI-D-17-0167.1.

733 Gu, L., P. J. Hanson, W. Mac Post, D. P. Kaiser, B. Yang, R. Nemani, S. G. Pallardy, and T.
734 Meyers, 2008: The 2007 eastern US spring freeze: Increased cold damage in a warming
735 world? *Bioscience*, **58**, 253–262, doi: 10.1641/B580311.

736 Guirguis, K., A. Gershunov, R. Schwartz, and S. Bennett, 2011: Recent warm and cold daily
737 winter temperature extremes in the Northern Hemisphere. *Geophys. Res. Lett.*, **38**,
738 L17701, doi: 10.1029/2011GL048762.

739 Hartjenstein, G., and R. Bleck, 1991: Factors affecting cold-air outbreaks east of the Rocky
740 Mountains. *Mon. Wea. Rev.*, **119**, 2280–2292, doi: 10.1175/1520-
741 0493(1991)119<2280:FACAOE>2.0.CO;2.

742 Hartmann, D. L., 2015: Pacific sea surface temperature and the winter of 2014. *Geophys. Res.*
743 *Lett.*, **42**, 1894–1902, doi: 10.1002/2015GL063083.

744 Higgins, R. W., A. Leetmaa, and V. E. Kousky, 2002: Relationships between climate variability
745 and winter temperature extremes in the United States. *J. Climate*, **15**, 1555–1572, doi:
746 10.1175/1520-0442(2002)015<1555:RBCVAW>2.0.CO;2.

747 Hoerling, M., A. Kumar, R. Dole, J. W. Nielsen-Gammon, J. Eischeid, J. Perlwitz, X.-W. Quan,
748 T. Zhang, P. Pegion, and M. Chen, 2013: Anatomy of an extreme event. *J. Climate*, **26**,
749 2811–2832, doi: 10.1175/JCLI-D-12-00270.1.

750 Isard, S. A., J. R. Angel, and G. T. VanDyke, 2000: Zones of origin for Great Lakes cyclones in
751 North America, 1899–1996. *Mon. Wea. Rev.*, **128**, 474–485, doi: 10.1175/1520-
752 0493(2000)128<0474:ZOOFGL>2.0.CO;2.

753 Jaffe, S. C., J. E. Martin, D. J. Vimont, and D. J. Lorenz, 2011: A synoptic climatology of
754 episodic, subseasonal retractions of the Pacific jet. *J. Climate*, **24**, 2846–2860, doi:
755 10.1175/2010JCLI3995.1.

756 Kenyon, J., and G. C. Hegerl, 2008: Influence of modes of climate variability on global
757 temperature extremes. *J. Climate*, **21**, 3872–3889, doi: 10.1175/2008JCLI2125.1.

758 Konrad, C. E., II, 1996: Relationships between the intensity of cold-air outbreaks and the
759 evolution of synoptic and planetary-scale features over North America. *Mon. Wea. Rev.*,
760 **124**, 1067–1083, doi: 10.1175/1520-0493(1996)124<1067:RBTIOC>2.0.CO;2.

761 Konrad, C. E., II, and S. J. Colucci, 1989: An examination of extreme cold air outbreaks over
762 eastern North America. *Mon. Wea. Rev.*, **117**, 2687–2700, doi: 10.1175/1520-
763 0493(1989)117<2687:AEOECA>2.0.CO;2.

764 Lim, Y.-K., and S. D. Schubert, 2011: The impact of ENSO and the Arctic Oscillation on winter
765 temperature extremes in the southeast United States. *Geophys. Res. Lett.*, **38**, L15706,
766 doi: 10.1029/2011GL048283.

767 Loikith, P. C., and A. J. Broccoli, 2012: Characteristics of observed atmospheric circulation
768 patterns associated with temperature extremes over North America. *J. Climate*, **25**, 7266–
769 7281, doi: 10.1175/JCLI-D-11-00709.1.

770 Loikith, P. C., and A. J. Broccoli, 2014: The influence of recurrent modes of climate variability
771 on the occurrence of winter and summer extreme temperatures over North America. *J.*
772 *Climate*, **27**, 1600–1618, doi: 10.1175/JCLI-D-13-00068.1.

773 Loikith, P. C., B. R. Lintner, and A. Sweeney, 2017: Characterizing large-scale meteorological
774 patterns and associated temperature and precipitation extremes over the northwestern
775 United States using self-organizing maps. *J. Climate*, **30**, 2829–2847, doi: 10.1175/JCLI-
776 D-16-0670.1.

777 Madonna, E., H. Wernli, H. Joos, and O. Martius, 2014: Warm conveyor belts in the ERA-
778 Interim dataset (1979–2010). Part I: Climatology and potential vorticity evolution. *J.*
779 *Climate*, **27**, 3–26, doi: 10.1175/JCLI-D-12-00720.1.

780 Massacand, A. C., H. Wernli, and H. C. Davies, 2001: Influence of upstream diabatic heating
781 upon an alpine event of heavy precipitation. *Mon. Wea. Rev.*, **129**, 2822–2828, doi:
782 10.1175/1520-0493(2001)129<2822:IOUDHU>2.0.CO;2.

783 Matsueda, S., and Y. Takaya, 2015: Global influence of the Madden–Julian Oscillation on
784 extreme temperature events. *J. Climate*, **28**, 4141–4151, doi: 10.1175/JCLI-D-14-
785 00625.1.

786 Meehl, G. A., and C. Tebaldi, 2004: More intense, more frequent, and longer lasting heat waves
787 in the 21st century. *Science*, **305**, 994–997, doi: 10.1126/science.1098704.

788 Meehl, G. A., C. Tebaldi, H. Teng, and T. C. Peterson, 2007: Current and future U.S. weather
789 extremes and El Niño. *Geophys. Res. Lett.*, **34**, L20704, doi: 10.1029/2007GL031027.

790 Moore, B. J., 2017: Rossby wave breaking and widespread extreme precipitation events in the
791 central and eastern U.S. Ph.D. Dissertation, University at Albany, SUNY, 188 pp.

792 Moore, B. J., K. M. Mahoney, E. M. Sukovich, R. Cifelli, and T. M. Hamill, 2015: Climatology
793 and environmental characteristics of extreme precipitation events in the southeastern
794 United States. *Mon. Wea. Rev.*, **143**, 718–741, doi: 10.1175/MWR-D-14-00065.1.

795 Mundhenk, B. D., E. A. Barnes, and E. D. Maloney, 2016: All-season climatology and
796 variability of atmospheric river frequencies over the North Pacific. *J. Climate*, **29**, 4885–
797 4903, doi: 10.1175/JCLI-D-15-0655.1.

798 Namias, J., 1978: Multiple causes of the North American abnormal winter 1976–77. *Mon. Wea.*
799 *Rev.*, **106**, 279–295, doi: 10.1175/1520-0493(1978)106<0279:MCOTNA>2.0.CO;2.

800 NWS, 2018: NWS Weather Fatality, Injury, and Damage Statistics. Accessed 27 August 2018,
801 <http://www.nws.noaa.gov/om/hazstats.shtml>.

802 Neiman, P. J., F. M. Ralph, G. A. Wick, J. D. Lundquist, and M. D. Dettinger, 2008:
803 Meteorological characteristics and overland precipitation impacts of atmospheric rivers
804 affecting the west coast of North America based on eight years of SSM/I satellite
805 observations. *J. Hydrometeor.*, **9**, 22–47, doi: 10.1175/2007JHM855.1.

806 North, G. R., T. L. Bell, R. F. Cahalan, and F. J. Moeng, 1982: Sampling errors in the estimation
807 of empirical orthogonal functions. *Mon. Wea. Rev.*, **110**, 699–706, doi: 10.1175/1520-
808 0493(1982)110<0699:SEITEO>2.0.CO;2.

809 Peterson, T. C., M. P. Hoerling, P. A. Stott, and S. C. Herring, 2013: Explaining extreme events
810 of 2012 from a climate perspective. *Bull. Amer. Meteor. Soc.*, **94**, S1–S74, doi:
811 10.1175/BAMS-D-13-00085.1.

812 Peterson, A. G., and J. T. Abatzoglou, 2014: Observed changes in false springs over the
813 contiguous United States. *Geophys. Res. Lett.*, **41**, 2156–2162, doi:
814 10.1002/2014GL059266.

815 Pfahl, S., C. Schwierz, M. Croci-Maspoli, C. M. Grams, and H. Wernli, 2015: Importance of
816 latent heat release in ascending air streams for atmospheric blocking. *Nat. Geosci.*, **8**,
817 610–614, doi: 10.1038/ngeo2487.

818 Portis, D. H., M. P. Cellitti, W. L. Chapman, and J. E. Walsh, 2006: Low-frequency variability
819 and evolution of North American cold air outbreaks. *Mon. Wea. Rev.*, **134**, 579–597, doi:
820 10.1175/MWR3083.1.

821 Ralph, F. M., P. J. Neiman, and G. A. Wick, 2004: Satellite and CALJET aircraft observations of
822 atmospheric rivers over the eastern North Pacific Ocean during the winter of 1997/98.

823 *Mon. Wea. Rev.*, **132**, 1721–1745, doi: 10.1175/1520-
824 0493(2004)132<1721:SACAOO>2.0.CO;2.

825 Rex, D. F., 1950: Blocking action in the middle troposphere and its effect upon regional climate.
826 I: An aerological study of blocking action. *Tellus*, **2A**, 196–211, doi: 10.1111/j.2153-
827 3490.1950.tb00331.x.

828 Riemer, M., S. C. Jones, and C. A. Davis, 2008: The impact of extratropical transition on the
829 downstream flow: An idealized modelling study with a straight jet. *Quart. J. Roy.*
830 *Meteor. Soc.*, **134**, 69–91, doi: 10.1002/qj.189.

831 Rogers, J. C., and R. V. Rohli, 1991: Florida citrus freezes and polar anticyclones in the Great
832 Plains. *J. Climate*, **4**, 1103–1113, doi: 10.1175/1520-0442(1991)004<1103:FCFAPA>
833 2.0.CO;2.

834 Roundy, P. E., N. Sakaeda, K. MacRitchie, and L. Gloeckler, 2017: Weather-climate interactions
835 and MJO influences. *Climate Extremes: Patterns and Mechanisms*, S.-Y. S. Wang, J.-H.
836 Yoon, C. C. Funk, and R. R. Gillies, Eds., American Geophysical Union, 139–163, doi:
837 10.1002/9781119068020.ch9.

838 Saha, S., and Coauthors, 2010: The NCEP Climate Forecast System Reanalysis. *Bull. Amer.*
839 *Meteor. Soc.*, **91**, 1015–1057, doi: 10.1175/2010BAMS3001.1.

840 Saha, S., and Coauthors, 2014: The NCEP Climate Forecast System version 2. *J. Climate*, **27**,
841 2185–2208, doi: 10.1175/JCLI-D-12-00823.1.

842 Sanders, F. and J. R. Gyakum, 1980, Synoptic-dynamic climatology of the “bomb.” *Mon. Wea.*
843 *Rev.*, **108**, 1589–1606, doi: 10.1175/1520-0493(1980)108<1589:SDCOT>2.0.CO;2.

844 Scherer, M., and N. S. Diffenbaugh, 2014: Transient twenty-first century changes in daily-scale
845 temperature extremes in the United States. *Climate Dyn.*, **42**, 1383–1404, doi:
846 10.1007/s00382-013-1829-2.

847 Thompson, D. W. J., and J. M. Wallace, 1998: The Arctic oscillation signature in wintertime
848 geopotential height and temperature fields. *Geophys. Res. Lett.*, **25**, 1297–1300, doi:
849 10.1029/98GL00950.

850 Tippett, M. K., J. T. Allen, V. A. Gensini, and H. E. Brooks, 2015: Climate and hazardous
851 convective weather. *Curr. Climate Change Rep.*, **1**, 60–73, doi: 10.1007/s40641-015-
852 0006-6.

853 Torn, R. D., 2010: Diagnosis of the downstream ridging associated with extratropical transition
854 using short-term ensemble forecasts. *J. Atmos. Sci.*, **67**, 817–833, doi:
855 10.1175/2009JAS3093.1.

856 Torn, R. D., and G. J. Hakim, 2015: Comparison of wave packets associated with extratropical
857 transition and winter cyclones. *Mon. Wea. Rev.*, **143**, 1782–1803, doi: 10.1175/MWR-D-
858 14-00006.1.

859 Turner, J. K., and J. R. Gyakum, 2011: The development of arctic air masses in northwest
860 Canada and their behavior in a warming climate. *J. Climate*, **24**, 4618–4633, doi:
861 10.1175/2011JCLI3855.1.

862 Vavrus, S., J. E. Walsh, W. L. Chapman, and D. Portis, 2006: The behavior of extreme cold air
863 outbreaks under greenhouse warming. *Int. J. Climatol.*, **26**, 1133–1147, doi:
864 10.1002/joc.1301.

865 Walsh, J. E., A. S. Phillips, D. H. Portis, and W. L. Chapman, 2001: Extreme cold outbreaks in
866 the United States and Europe, 1948–99. *J. Climate*, **14**, 2642–2658, doi: 10.1175/1520-
867 0442(2001)014<2642:ECOITU>2.0.CO;2.

868 Wheeler, M. C., and H. H. Hendon, 2004: An all-season real-time multivariate MJO index:
869 Development of an index for monitoring and prediction. *Mon. Wea. Rev.*, **132**, 1917–
870 1932, doi: 10.1175/1520-0493(2004)132<1917:AARMMI>2.0.CO;2.

871 Wilks, D. S., 2011: *Statistical Methods in the Atmospheric Sciences*. 3rd ed. Elsevier, 676 pp.

872 Winters, A. C., D. Keyser, and L. F. Bosart, 2018: The development of the North Pacific Jet
873 Phase Diagram as an objective tool to monitor the state of the upper-tropospheric flow
874 pattern. *Wea. Forecasting*, **33**, (in review).

875 Westby, R. M., Y.-Y. Lee, and R. X. Black, 2013: Anomalous temperature regimes during the
876 cool season: Long-term trends, low-frequency mode modulation, and representation in
877 CMIP5 simulations. *J. Climate*, **26**, 9061–9076, doi: 10.1175/JCLI-D-13-00003.1.

878 Westby, R. M., and R. X. Black, 2015: Development of anomalous temperature regimes over the
879 southeastern United States: Synoptic behavior and role of low-frequency modes. *Wea.*
880 *Forecasting*, **30**, 553–570, doi: 10.1175/WAF-D-14-00093.1.

881 Wolter, K., M. Hoerling, J. K. Eischeid, G. J. van Oldenborgh, X.-W. Quan, J. E. Walsh, T. N.
882 Chase, and R. M. Dole, 2015: How unusual was the cold winter of 2013/14 in the Upper
883 Midwest? *Bull. Amer. Meteor. Soc.*, **96**, S10–S14, doi: 10.1175/BAMS-D-15-00126.1.

884 Xie, Z., R. X. Black, and Y. Deng, 2017: Daily-scale planetary wave patterns and the modulation
885 of cold season weather in the northern extratropics. *J. Geophys. Res. Atmos.*, **122**, 8383–
886 8398, doi: 10.1002/2017JD026768.

887 Zhang, C., 2016: MJO and extreme weather/climate events. *Dynamics and Predictability of*
888 *Large-Scale, High-Impact Weather and Climate Events*, J. Li, R. Swinbank, R. Grotjahn,
889 and H. Volkert, Eds., Cambridge University Press, 294–300, doi:
890 10.1017/CBO9781107775541.025.

891 Zhu, Y., and R. E. Newell, 1998: A proposed algorithm for moisture fluxes from atmospheric
892 rivers. *Mon. Wea. Rev.*, **126**, 725–735, doi: 10.1175/1520-
893 0493(1998)126<0725:APAFMF>2.0.CO;2.

894

895

896

897

898

899

900

901

902

903

904

905

906

907

908

909

910 **Table Captions**

911 TABLE 1. Modes of intraannual and interannual climate variability and selected studies that
912 have sought relationships between these modes of variability and cool season ETEs.

913

914 TABLE 2. The characteristics of continental U.S. ETEs identified during the 36-year period,
915 1979–2014. The characteristics provided include the minimum gridpoint thresholds required for
916 the identification of an ETE within the eastern and western U.S. domains, the total number of
917 ETEs identified within the eastern and western U.S. domains, and the number of ETEs that
918 occurred during the cool season. Refer to the text for a full discussion of the ETE identification
919 scheme.

920

921

922

923

924

925

926

927

928

929

930

931

932

933 **Tables**

Modes of Climate Variability	Citations
Pacific–North American Pattern	Rogers and Rohli (1991); Downton and Miller (1993); Cellitti et al. (2006); Westby et al. (2013); Loikith and Broccoli (2014); Westby and Black (2015)
North Atlantic Oscillation	Downton and Miller (1993); Cellitti et al. (2006); Kenyon and Hegerl (2008); Guirguis et al. (2011); Westby et al. (2013); Westby and Black (2015)
Arctic Oscillation	Higgins et al. (2002); Lim and Schubert (2011); Loikith and Broccoli (2014)
Madden–Julian Oscillation	Matsueda and Takaya (2015); Zhang (2016); Roundy et al. (2017)
Pacific Decadal Oscillation	Guirguis et al. (2011); Westby et al. (2013); Xie et al. (2017)
El Niño–Southern Oscillation	Namias (1978); Higgins et al. (2002); Carrera et al. (2004); Meehl et al. (2007); Kenyon and Hegerl (2008); Guirguis et al. (2011); Lim and Schubert (2011); Westby et al. (2013); Loikith and Broccoli (2014); Xie et al. (2017)

934

935 **TABLE 1.** Modes of intraannual and interannual climate variability and selected studies that
 936 have sought relationships between these modes of variability and cool season ETEs.
 937

938

939

940

941

942

943

944

945

946

947

948

949

Extreme Temperature Events				
	Spatial Domain	Min. Gridpoint Threshold	Total Number of Identified Events	Cool Season Events
Extreme Warm Events	East	224	304	239
	West	144	264	204
Extreme Cold Events	East	221	225	173
	West	125	269	196

950

951 TABLE 2. The characteristics of continental U.S. ETEs identified during the 36-year period,
 952 1979–2014. The characteristics provided include the minimum gridpoint thresholds required for
 953 the identification of an ETE within the eastern and western U.S. domains, the total number of
 954 ETEs identified within the eastern and western U.S. domains, and the number of ETEs that
 955 occurred during the cool season. Refer to the text for a full discussion of the ETE identification
 956 scheme.

957

958

959

960

961

962

963

964

965

966

967

968

969

970

971 **Figure Captions**

972 FIG. 1. (a) Frequency distribution of 2-m temperatures compiled at 24-h intervals within a 21-
973 day window centered on 1900 UTC 30 May for every year between 1979 and 2014 for a grid
974 point near Albany, NY (43°N, 74°W). The vertical black bar identifies the 99th-percentile
975 temperature of the distribution and the quantity in the top left of the panel indicates the total
976 number of 1-h forecasts that are used to construct the distribution. (b) 99th-percentile
977 temperature at 1900 UTC 30 May is shaded in the fill pattern. The black boxes identify the
978 eastern and western U.S. domains used to identify continental U.S. ETEs. (c) Frequency
979 distribution of the number of grid points characterized by extreme warmth within the subset of 1-
980 h forecasts during 1979–2014 that exhibit at least one grid point over land in the eastern U.S.
981 domain with a 2-m temperature greater than its respective 99th-percentile temperature. The
982 vertical black bar identifies the number of grid points corresponding to the 95th percentile of the
983 distribution. The black arrow identifies the maximum number of grid points characterized by
984 extreme warmth in a single 1-h forecast during 1979–2014.

985

986 FIG. 2. (a) The number of eastern U.S. extreme warm events during the cool season that initiate
987 at each grid point is shaded in the fill pattern. Individual extreme warm event centroids are
988 represented by dots and are colored according to their respective geographic cluster. (b) As in
989 (a), but for extreme warm events that initiate within the western U.S. domain during the cool
990 season.

991

992 FIG. 3. As in Fig. 2, but for extreme cold events that initiate within the (a) eastern U.S. domain
993 and (b) western U.S. domain during the cool season.

994

995 FIG. 4. (a) September–May 250-hPa mean zonal wind is contoured in black every 10 m s^{-1}
996 above 30 m s^{-1} , and the regression of 250-hPa zonal wind anomaly data onto standardized PC 1
997 (i.e., EOF 1) is shaded in m s^{-1} . The variance of 250-hPa zonal wind during the cool season that
998 is explained by EOF 1 is listed in the top right of the panel. (b) As in (a), but for the regression of
999 250-hPa zonal wind anomaly data onto standardized PC 2 (i.e., EOF 2). Figure and caption from
1000 Winters et al. (2018).

1001

1002 FIG. 5. Schematic illustrating the NPJ Phase Diagram and the classification scheme used to
1003 determine the NPJ regime prior to ETE initiation. The values plotted on the axes of the NPJ
1004 Phase Diagram correspond to the value of weighted PC 1 and weighted PC 2, respectively.

1005

1006 FIG. 6. Composite mean 250-hPa wind speed in m s^{-1} is shaded in the fill pattern, 250-hPa
1007 geopotential height is contoured in black every 120 m, and 250-hPa geopotential height
1008 anomalies are contoured in solid red and dashed blue every 30 m for positive and negative
1009 values, respectively, 4 days following the initiation of (a) a jet extension, (b) a jet retraction, (c) a
1010 poleward shift, and (d) an equatorward shift regime. The numbers in the bottom right of each
1011 panel indicate the number of cases included in each composite and stippled areas represent
1012 locations where the 250-hPa geopotential height anomalies are statistically distinct from
1013 climatology at the 99% confidence level using a two-sided Student's t test. Figure and caption
1014 adapted from Winters et al. (2018).

1015

1016 FIG. 7. Composite anomalies of mean sea-level pressure are contoured in solid and dashed black
1017 every 2 hPa for positive and negative values, respectively, and 850-hPa temperature anomalies
1018 are shaded in the fill pattern every 1 K 4 days following the initiation of (a) a jet extension, (b) a
1019 jet retraction, (c) a poleward shift, and (d) an equatorward shift regime. The numbers in the
1020 bottom right of each panel indicate the number of cases included in each composite and stippled
1021 areas represent locations where the 850-hPa temperature anomalies are statistically distinct from
1022 climatology at the 99% confidence level using a two-sided Student's t test. Figure and caption
1023 adapted from Winters et al. (2018).

1024

1025 FIG. 8. (a) The number of eastern U.S. extreme warm events during the cool season (Sep–May),
1026 fall (Sep–Nov), winter (Dec–Feb), and spring (Mar–May) associated with each NPJ regime
1027 during the 3–7-day period prior to event initiation. The quantities listed above each bar indicate
1028 the number of events that are associated with a particular NPJ regime. As in (a), but for (b)
1029 Northern Plains, (c) Southern Plains, and (d) East Coast extreme warm events during the cool
1030 season.

1031

1032 FIG. 9. As in Fig. 8, but for (a) western U.S., (b) Pacific Northwest, (c) Northern Rockies, and
1033 (d) Southwest extreme warm events during the cool season.

1034

1035 FIG. 10. (a) Composite trajectory showing the evolution of the NPJ at 6-h intervals during the
1036 10-day period prior to event initiation for all eastern U.S. extreme warm events during the cool
1037 season and for extreme warm events within the three eastern U.S. geographic clusters. All
1038 trajectories are colored by geographic cluster according to the legend and are shifted such that

1039 they begin at the origin of the NPJ Phase Diagram 10 days prior to event initiation. The colored
1040 diamonds offset from the origin of the NPJ Phase Diagram correspond to the end point of a
1041 particular trajectory at the time of event initiation. (b) As in (a), but for all western U.S. extreme
1042 warm events and for the extreme warm events within the three western U.S. geographic clusters.

1043

1044 FIG. 11. As in Fig. 8, but for (a) eastern U.S., (b) Northern Plains, (c) Northeast, (d) Southern
1045 Plains, and (e) Southeast extreme cold events during the cool season.

1046

1047 FIG. 12. As in Fig. 8, but for (a) western U.S., (b) Pacific Northwest, (c) Northern Rockies, and
1048 (d) Southwest extreme cold events during the cool season.

1049

1050 FIG. 13. As in Fig. 10, but for (a) all eastern U.S. and (b) all western U.S. extreme cold events
1051 during the cool season, and for those events within the four eastern U.S. and three western U.S.
1052 geographic clusters, respectively.

1053

1054 FIG. 14. Composite synoptic-scale flow evolution prior to the initiation of a Southern Plains
1055 extreme warm event following a jet retraction during the cool season. [left column] 250-hPa
1056 wind speed is shaded in m s^{-1} according to the legend, 250-hPa geopotential height is contoured
1057 in black every 12 dam, standardized 250-hPa geopotential height anomalies are contoured in
1058 solid and dashed yellow every 0.5σ for positive and negative values, respectively, and positive
1059 standardized precipitable water anomalies are shaded in green according to the legend (a) 6 days,
1060 (c) 4 days, (e) 2 days, and (g) 0 days prior to extreme warm event initiation. Stippled areas
1061 represent locations where the 250-hPa geopotential height anomalies are statistically distinct

1062 from climatology at the 99% confidence level. [right column] Standardized 850-hPa temperature
1063 anomalies are shaded every 0.5σ according to the legend, mean sea level pressure is contoured in
1064 black every 4 hPa, and 1000–500-hPa thickness is contoured in dashed red and blue for values
1065 greater than 540 dam and less than or equal to 540 dam, respectively, (b) 6 days, (d) 4 days, (f) 2
1066 days, and (h) 0 days prior to extreme warm event initiation. The red ‘L’s and blue ‘H’s identify
1067 the locations of surface cyclones and anticyclones. Stippled areas represent locations where the
1068 850-hPa temperature anomalies are statistically distinct from climatology at the 99% confidence
1069 level.

1070

1071

1072

1073

1074

1075

1076

1077

1078

1079

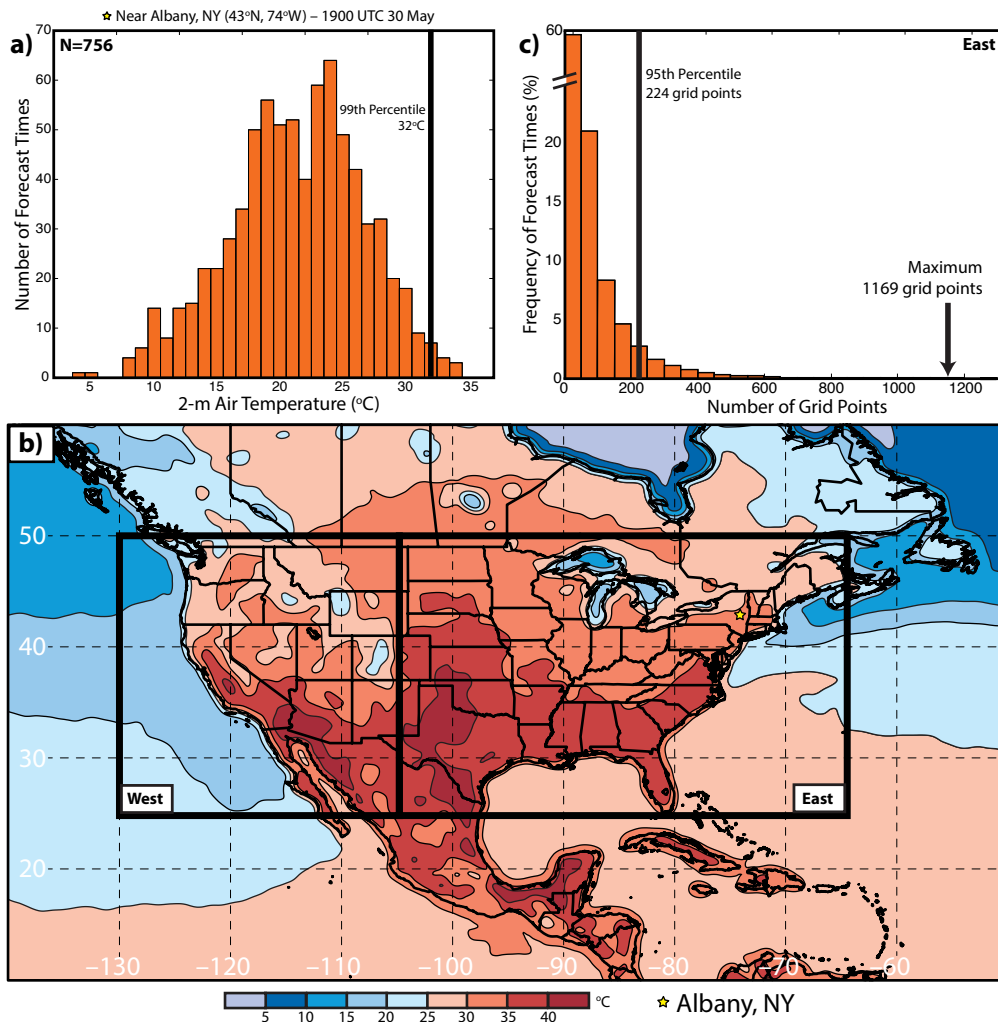
1080

1081

1082

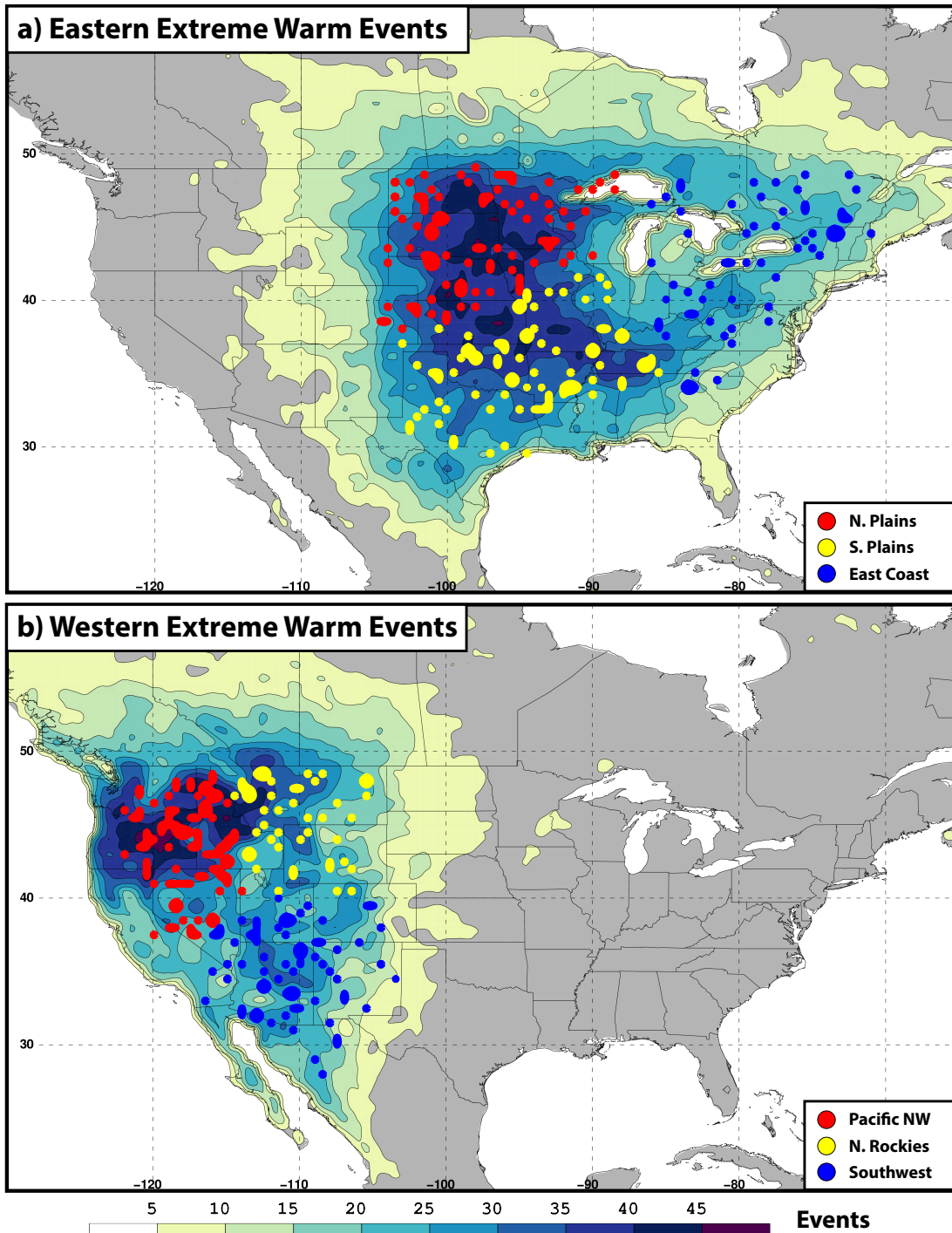
1083

1084



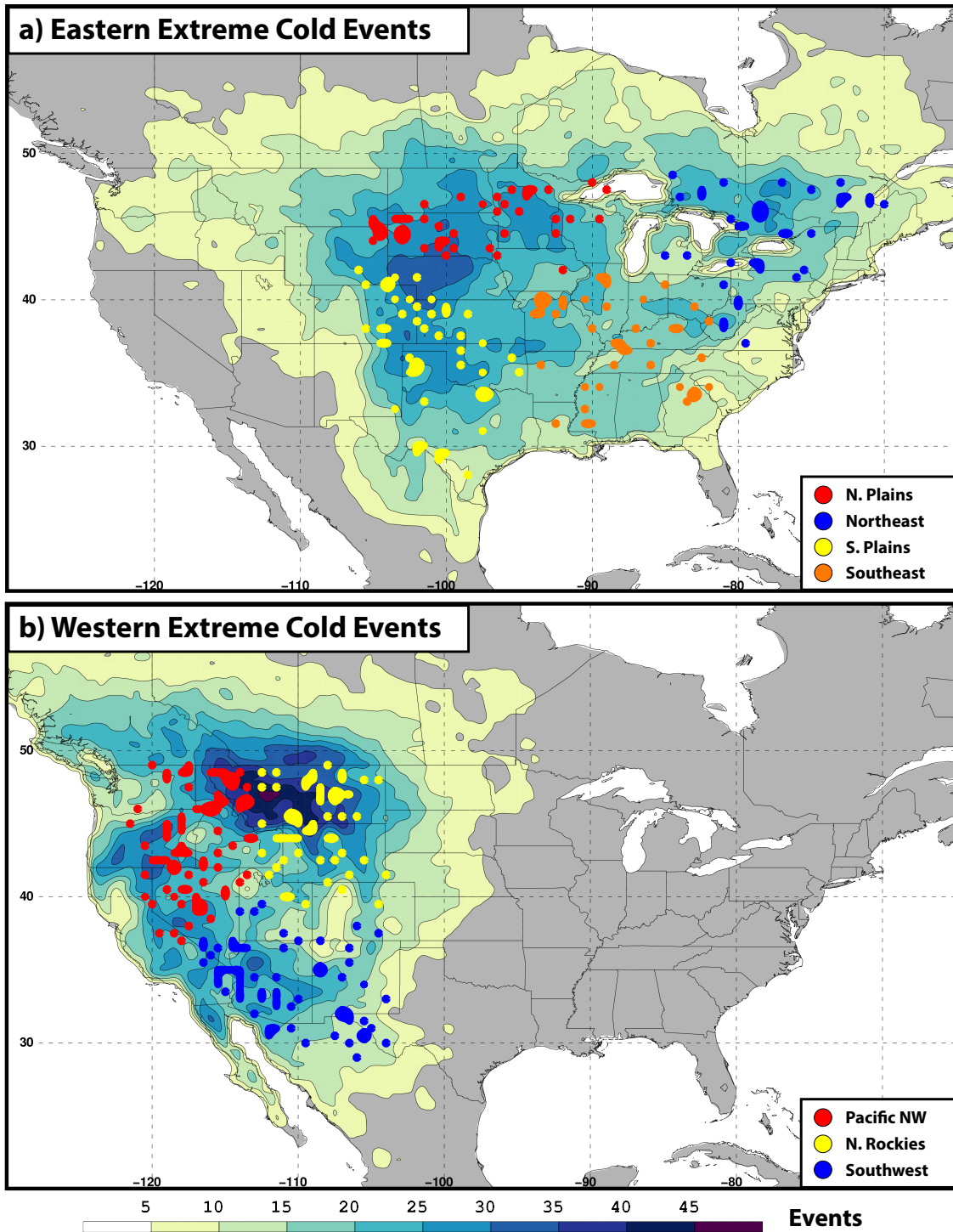
1086
 1087
 1088
 1089
 1090
 1091
 1092
 1093
 1094
 1095
 1096
 1097
 1098
 1099
 1100
 1101
 1102

FIG. 1. (a) Frequency distribution of 2-m temperatures compiled at 24-h intervals within a 21-day window centered on 1900 UTC 30 May for every year between 1979 and 2014 for a grid point near Albany, NY (43°N, 74°W). The vertical black bar identifies the 99th-percentile temperature of the distribution and the quantity in the top left of the panel indicates the total number of 1-h forecasts that are used to construct the distribution. (b) 99th-percentile temperature at 1900 UTC 30 May is shaded in the fill pattern. The black boxes identify the eastern and western U.S. domains used to identify continental U.S. ETEs. (c) Frequency distribution of the number of grid points characterized by extreme warmth within the subset of 1-h forecasts during 1979–2014 that exhibit at least one grid point over land in the eastern U.S. domain with a 2-m temperature greater than its respective 99th-percentile temperature. The vertical black bar identifies the number of grid points corresponding to the 95th percentile of the distribution. The black arrow identifies the maximum number of grid points characterized by extreme warmth in a single 1-h forecast during 1979–2014.



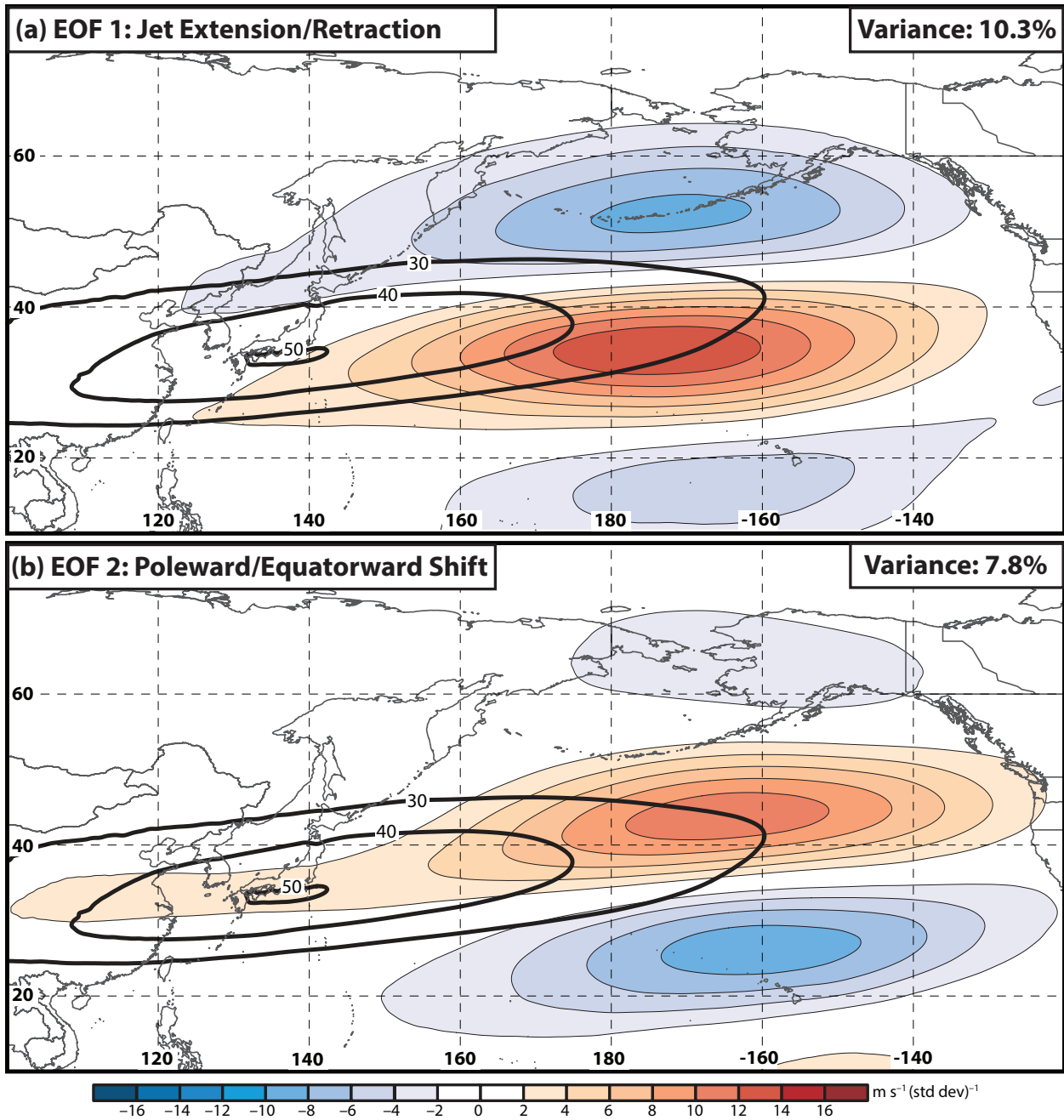
1103
 1104
 1105
 1106
 1107
 1108
 1109
 1110
 1111

FIG. 2. (a) The number of eastern U.S. extreme warm events during the cool season that initiate at each grid point is shaded in the fill pattern. Individual extreme warm event centroids are represented by dots and are colored according to their respective geographic cluster. (b) As in (a), but for extreme warm events that initiate within the western U.S. domain during the cool season.



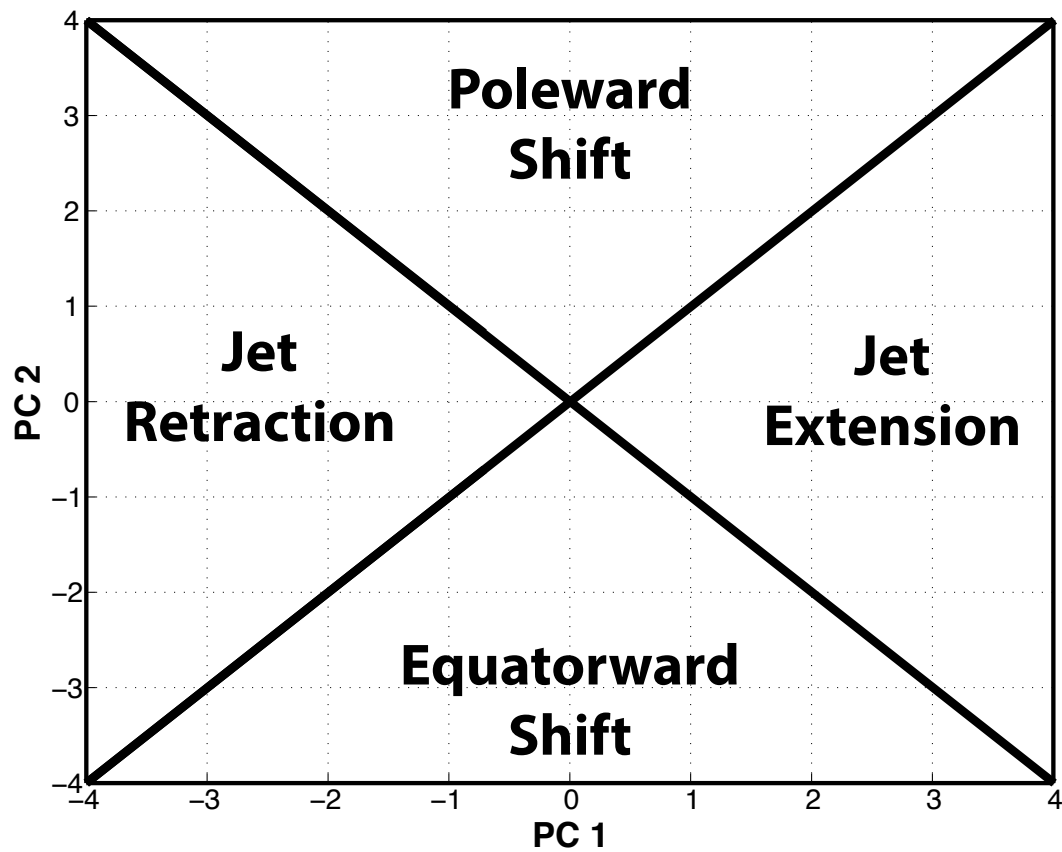
1112
 1113
 1114
 1115
 1116
 1117
 1118
 1119

FIG. 3. As in Fig. 2, but for extreme cold events that initiate within the (a) eastern U.S. domain and (b) western U.S. domain during the cool season.



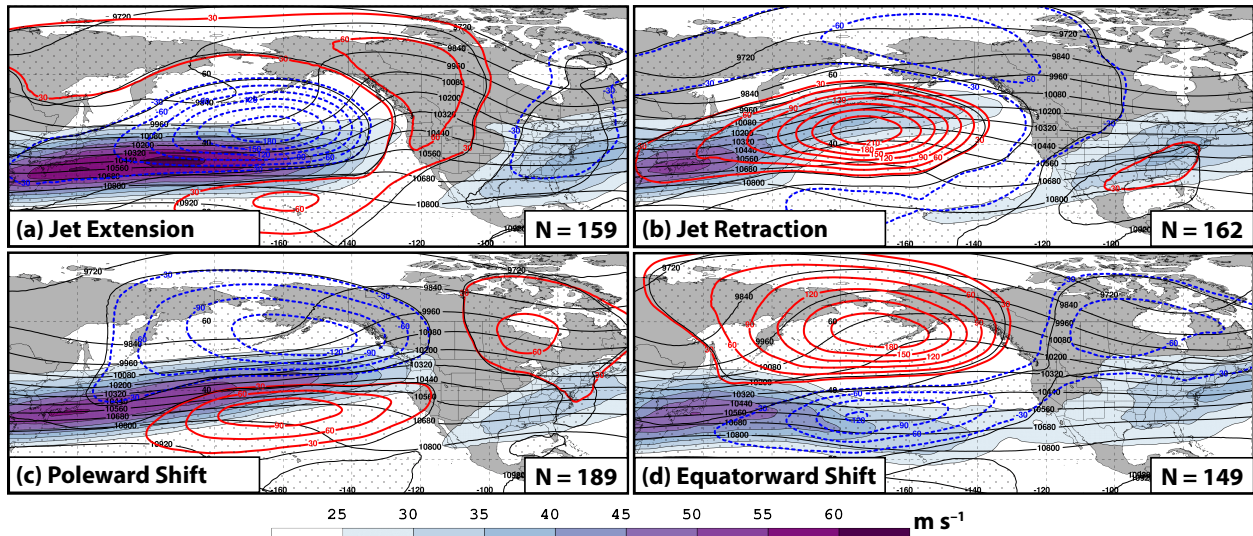
1120
 1121
 1122
 1123
 1124
 1125
 1126
 1127
 1128
 1129
 1130
 1131

FIG. 4. (a) September–May 250-hPa mean zonal wind is contoured in black every 10 m s^{-1} above 30 m s^{-1} , and the regression of 250-hPa zonal wind anomaly data onto standardized PC 1 (i.e., EOF 1) is shaded in m s^{-1} . The variance of 250-hPa zonal wind during the cool season that is explained by EOF 1 is listed in the top right of the panel. (b) As in (a), but for the regression of 250-hPa zonal wind anomaly data onto standardized PC 2 (i.e., EOF 2). Figure and caption from Winters et al. (2018).



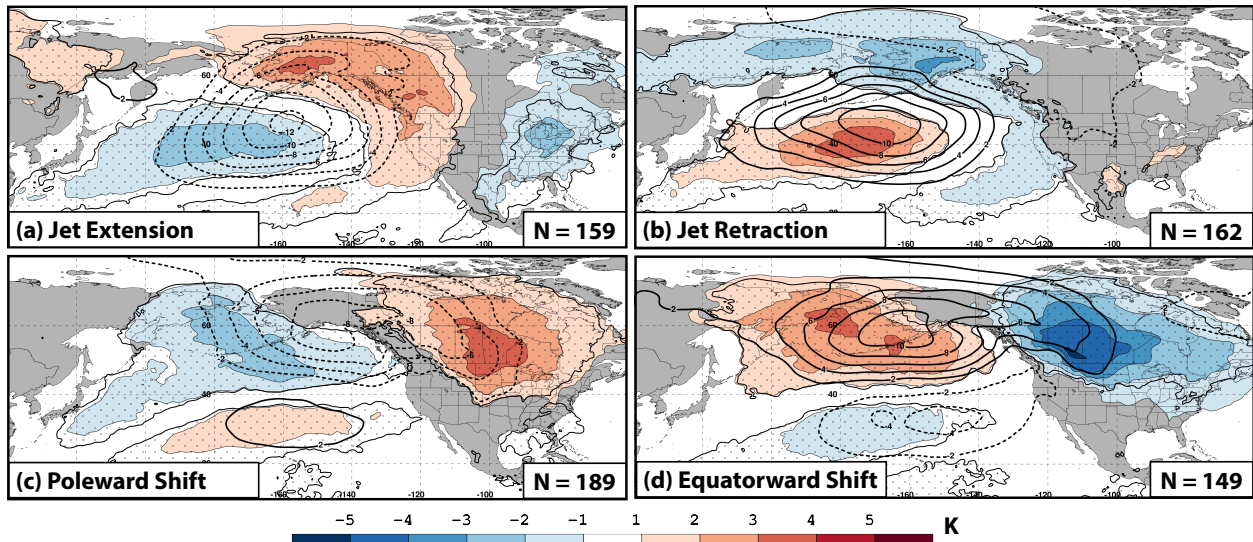
1132
 1133
 1134
 1135
 1136
 1137
 1138
 1139
 1140
 1141
 1142
 1143
 1144
 1145
 1146
 1147
 1148
 1149
 1150
 1151
 1152
 1153

FIG. 5. Schematic illustrating the NPJ Phase Diagram and the classification scheme used to determine the NPJ regime prior to ETE initiation. The values plotted on the axes of the NPJ Phase Diagram correspond to the value of weighted PC 1 and weighted PC 2, respectively.



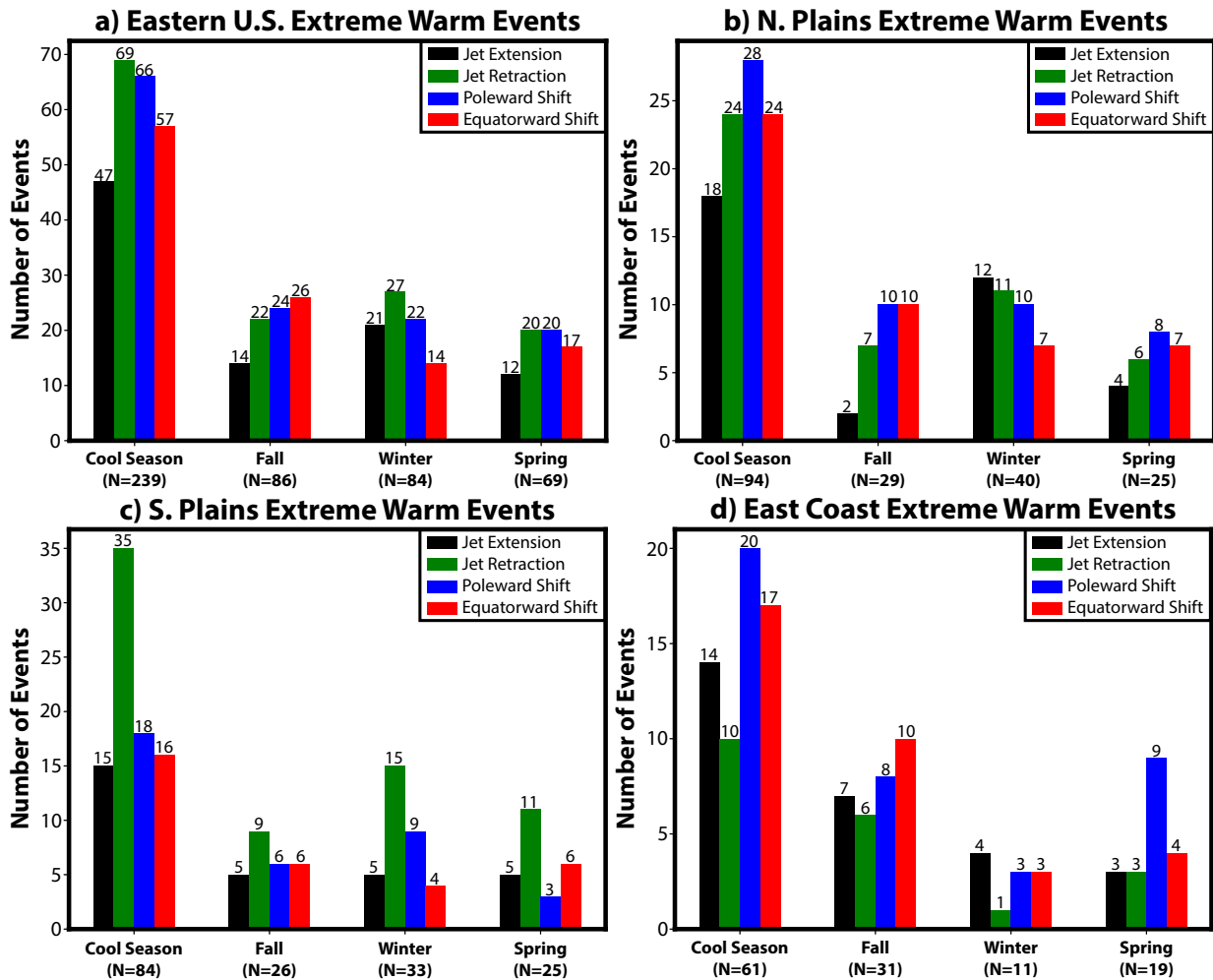
1154
 1155
 1156
 1157
 1158
 1159
 1160
 1161
 1162
 1163
 1164
 1165
 1166
 1167
 1168
 1169
 1170
 1171
 1172
 1173
 1174
 1175
 1176
 1177
 1178
 1179
 1180
 1181
 1182
 1183
 1184
 1185
 1186

FIG. 6. Composite mean 250-hPa wind speed in m s^{-1} is shaded in the fill pattern, 250-hPa geopotential height is contoured in black every 120 m, and 250-hPa geopotential height anomalies are contoured in solid red and dashed blue every 30 m for positive and negative values, respectively, 4 days following the initiation of (a) a jet extension, (b) a jet retraction, (c) a poleward shift, and (d) an equatorward shift regime. The numbers in the bottom right of each panel indicate the number of cases included in each composite and stippled areas represent locations where the 250-hPa geopotential height anomalies are statistically distinct from climatology at the 99% confidence level using a two-sided Student's t test. Figure and caption adapted from Winters et al. (2018).



1187
 1188
 1189
 1190
 1191
 1192
 1193
 1194
 1195
 1196
 1197
 1198
 1199
 1200
 1201
 1202
 1203
 1204
 1205
 1206
 1207
 1208
 1209
 1210
 1211
 1212
 1213
 1214
 1215
 1216
 1217
 1218

FIG. 7. Composite anomalies of mean sea-level pressure are contoured in solid and dashed black every 2 hPa for positive and negative values, respectively, and 850-hPa temperature anomalies are shaded in the fill pattern every 1 K 4 days following the initiation of (a) a jet extension, (b) a jet retraction, (c) a poleward shift, and (d) an equatorward shift regime. The numbers in the bottom right of each panel indicate the number of cases included in each composite and stippled areas represent locations where the 850-hPa temperature anomalies are statistically distinct from climatology at the 99% confidence level using a two-sided Student's t test. Figure and caption adapted from Winters et al. (2018).



1219
 1220
 1221
 1222
 1223
 1224
 1225
 1226
 1227
 1228
 1229
 1230
 1231
 1232
 1233
 1234
 1235
 1236
 1237
 1238

FIG. 8. (a) The number of eastern U.S. extreme warm events during the cool season (Sep–May), fall (Sep–Nov), winter (Dec–Feb), and spring (Mar–May) associated with each NPJ regime during the 3–7-day period prior to event initiation. The quantities listed above each bar indicate the number of events that are associated with a particular NPJ regime. As in (a), but for (b) Northern Plains, (c) Southern Plains, and (d) East Coast extreme warm events during the cool season.

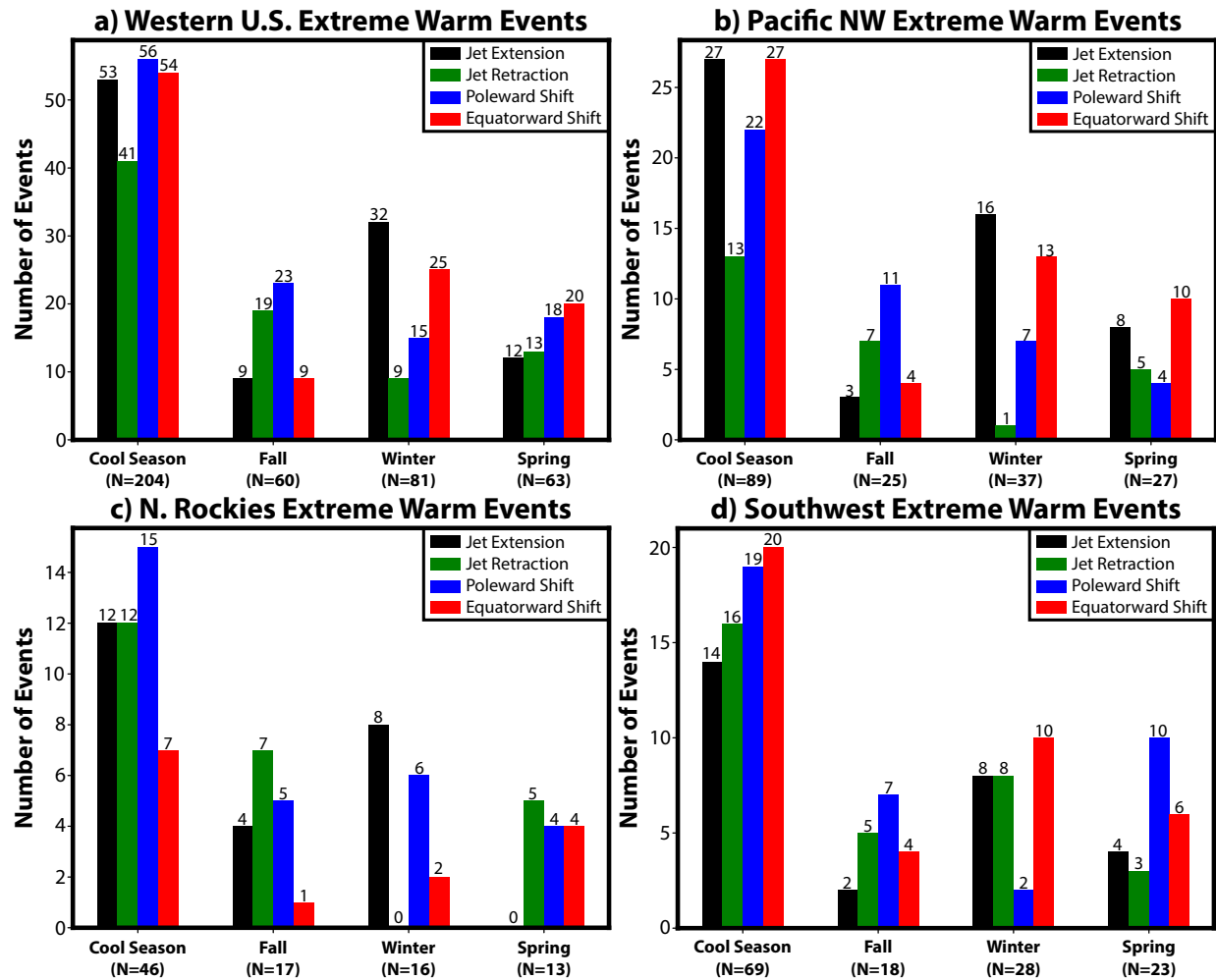
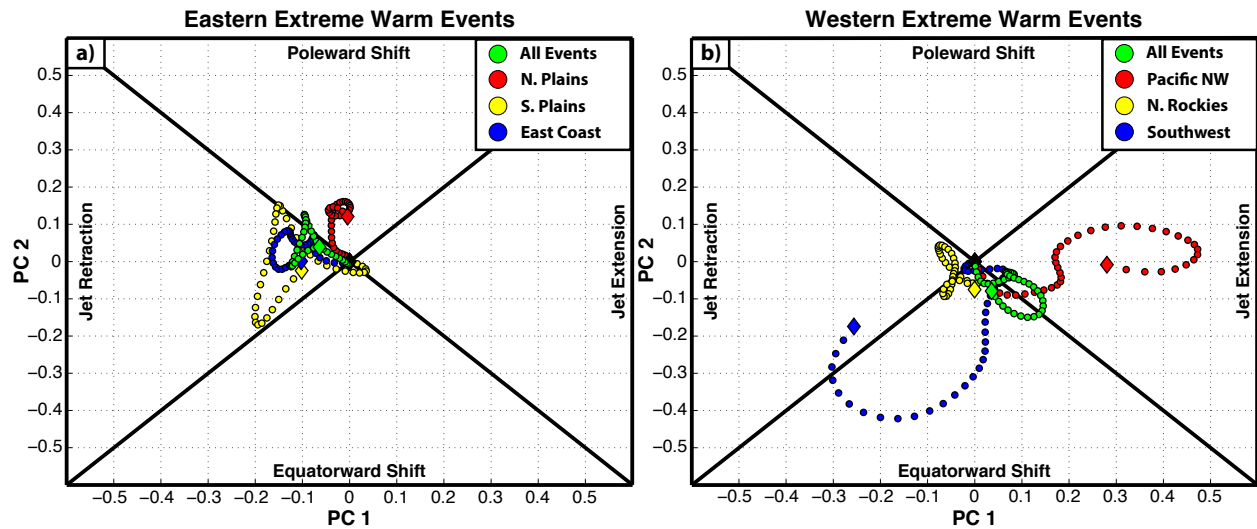


FIG. 9. As in Fig. 8, but for (a) western U.S., (b) Pacific Northwest, (c) Northern Rockies, and (d) Southwest extreme warm events during the cool season.

1239
 1240
 1241
 1242
 1243
 1244
 1245
 1246
 1247
 1248
 1249
 1250
 1251
 1252
 1253
 1254
 1255
 1256
 1257
 1258



1259
 1260
 1261
 1262
 1263
 1264
 1265
 1266
 1267
 1268
 1269
 1270
 1271
 1272
 1273
 1274
 1275
 1276
 1277
 1278
 1279
 1280
 1281
 1282
 1283
 1284
 1285
 1286
 1287
 1288
 1289
 1290
 1291

FIG. 10. (a) Composite trajectory showing the evolution of the NPJ at 6-h intervals during the 10-day period prior to event initiation for all eastern U.S. extreme warm events during the cool season and for extreme warm events within the three eastern U.S. geographic clusters. All trajectories are colored by geographic cluster according to the legend and are shifted such that they begin at the origin of the NPJ Phase Diagram 10 days prior to event initiation. The colored diamonds offset from the origin of the NPJ Phase Diagram correspond to the end point of a particular trajectory at the time of event initiation. (b) As in (a), but for all western U.S. extreme warm events and for the extreme warm events within the three western U.S. geographic clusters.

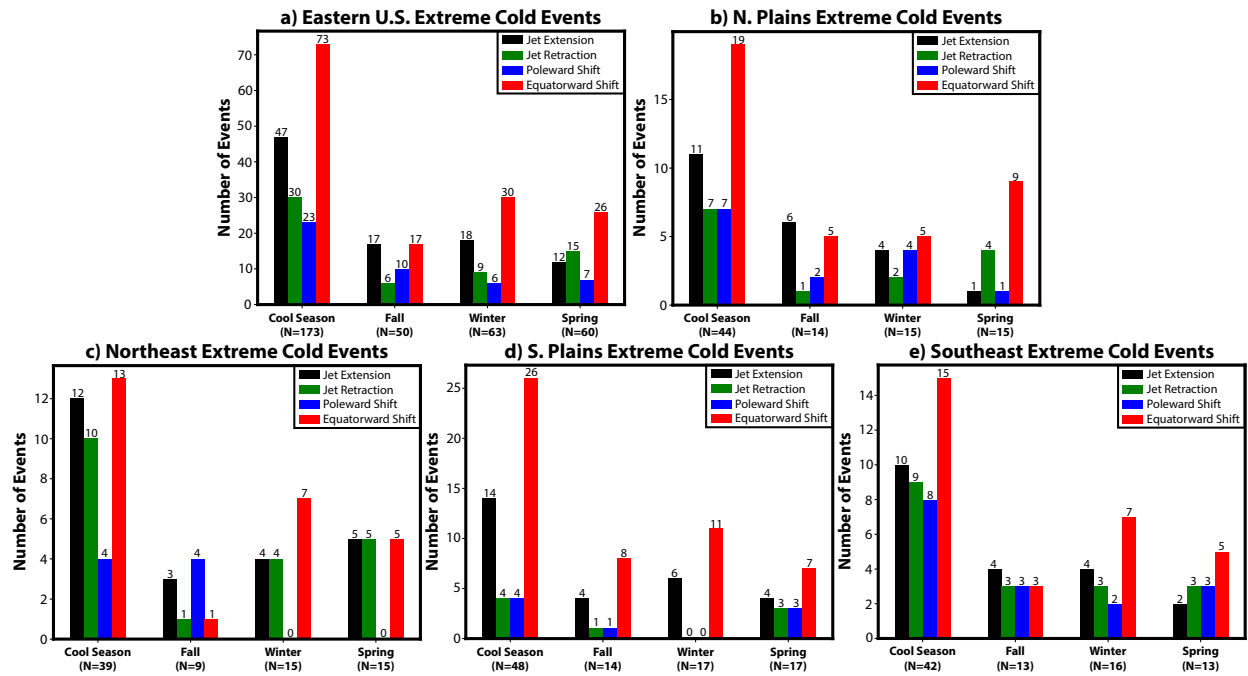


FIG. 11. As in Fig. 8, but for (a) eastern U.S., (b) Northern Plains, (c) Northeast, (d) Southern Plains, and (e) Southeast extreme cold events during the cool season.

1292
 1293
 1294
 1295
 1296
 1297
 1298
 1299
 1300
 1301
 1302
 1303
 1304
 1305
 1306
 1307
 1308
 1309
 1310
 1311
 1312
 1313
 1314
 1315
 1316
 1317
 1318
 1319
 1320

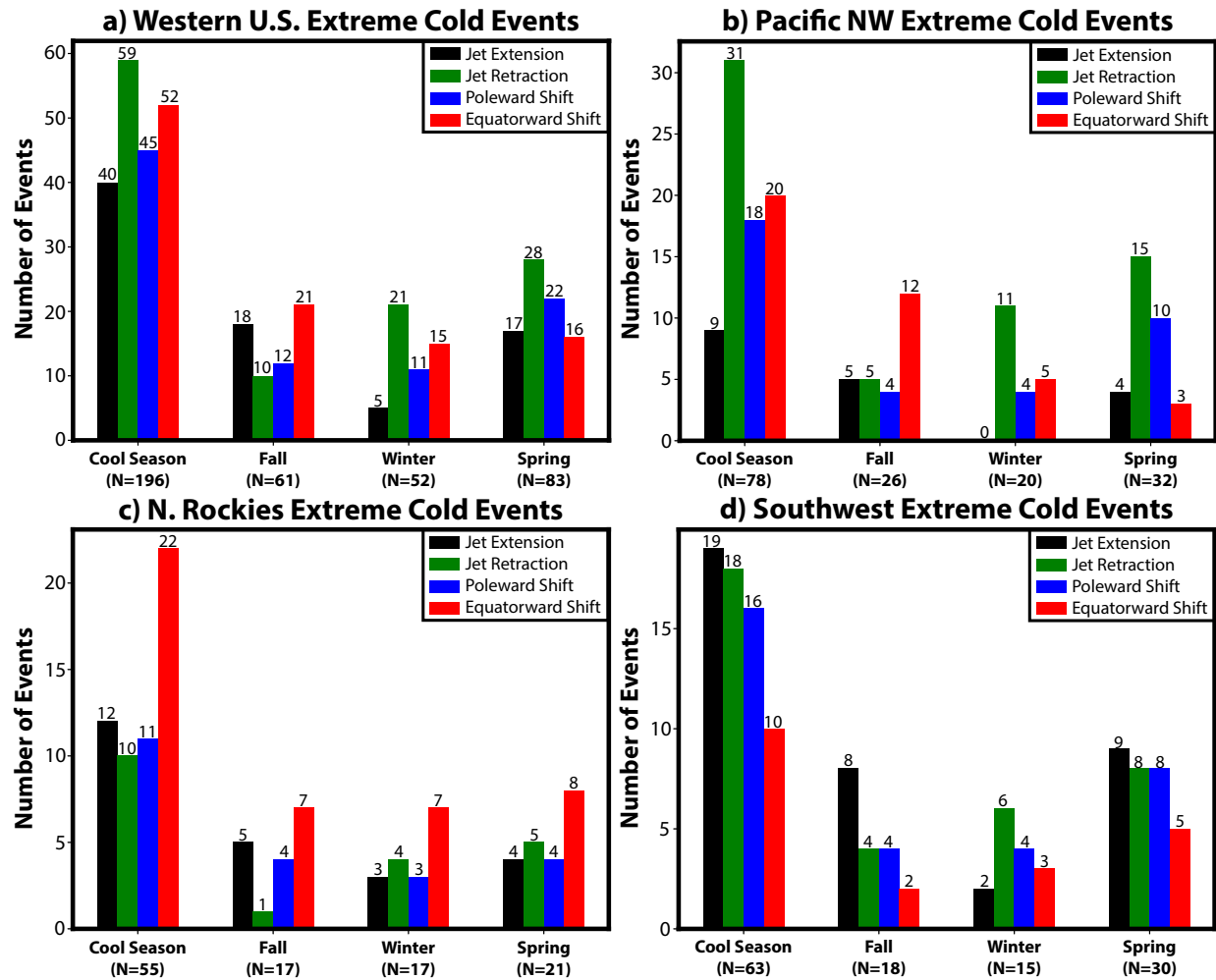


FIG. 12. As in Fig. 8, but for (a) western U.S., (b) Pacific Northwest, (c) Northern Rockies, and (d) Southwest extreme cold events during the cool season.

1321
 1322
 1323
 1324
 1325
 1326
 1327
 1328
 1329
 1330
 1331
 1332
 1333
 1334
 1335
 1336
 1337
 1338
 1339
 1340

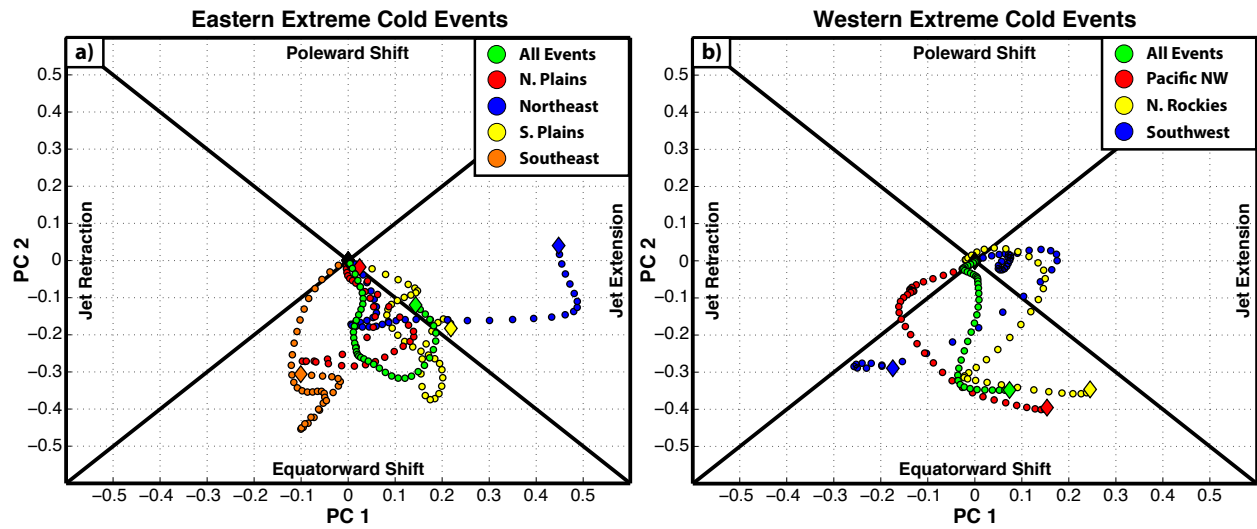
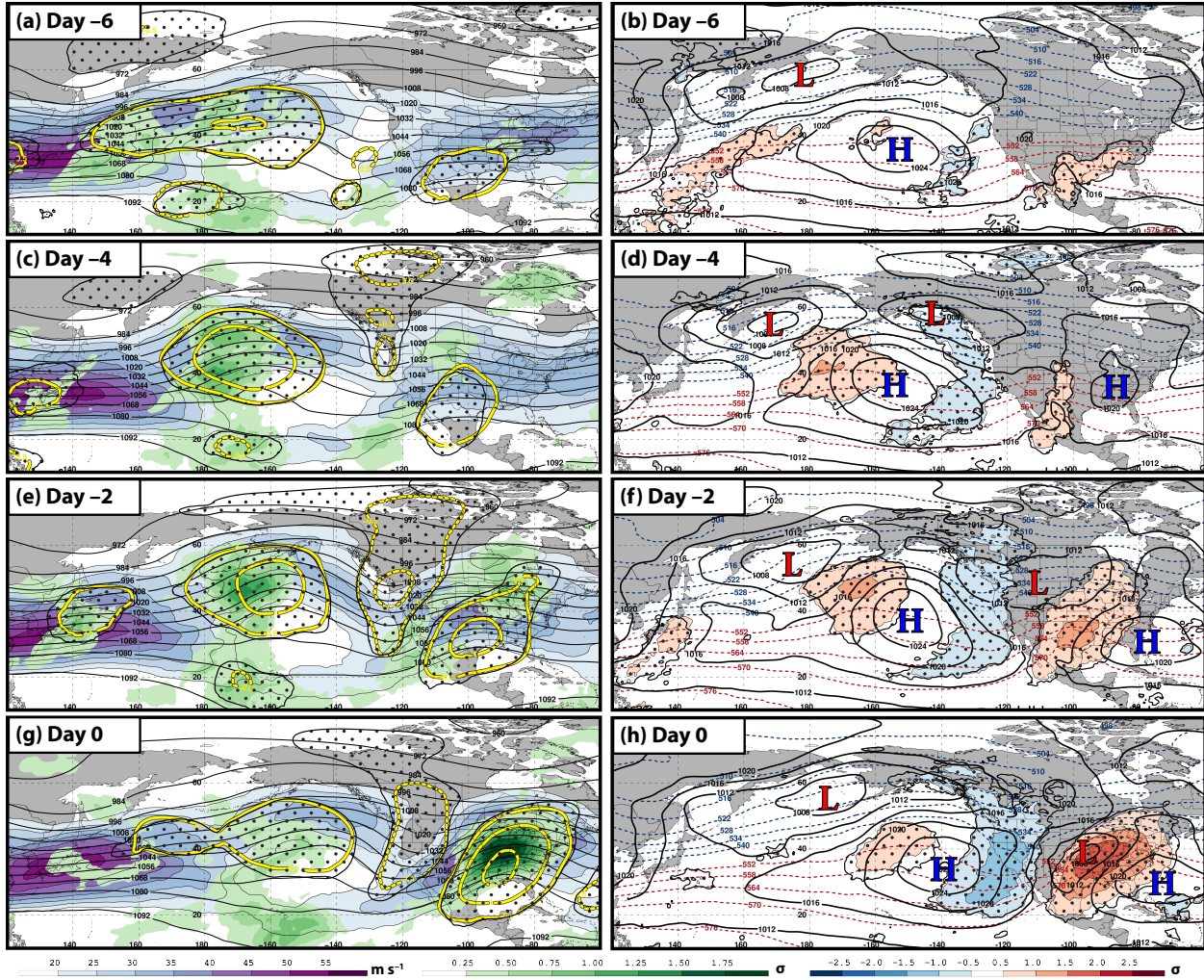


FIG. 13. As in Fig. 10, but for (a) all eastern U.S. and (b) all western U.S. extreme cold events during the cool season, and for those events within the four eastern U.S. and three western U.S. geographic clusters, respectively.

1341
 1342
 1343
 1344
 1345
 1346
 1347
 1348
 1349
 1350
 1351
 1352
 1353
 1354
 1355
 1356
 1357
 1358
 1359
 1360
 1361
 1362
 1363
 1364
 1365
 1366
 1367
 1368
 1369
 1370
 1371
 1372
 1373



1374
 1375
 1376
 1377
 1378
 1379
 1380
 1381
 1382
 1383
 1384
 1385
 1386
 1387
 1388
 1389
 1390
 1391
 1392

FIG. 14. Composite synoptic-scale flow evolution prior to the initiation of a Southern Plains extreme warm event following a jet retraction during the cool season. [left column] 250-hPa wind speed is shaded in m s^{-1} according to the legend, 250-hPa geopotential height is contoured in black every 12 dam, standardized 250-hPa geopotential height anomalies are contoured in solid and dashed yellow every 0.5σ for positive and negative values, respectively, and positive standardized precipitable water anomalies are shaded in green according to the legend (a) 6 days, (c) 4 days, (e) 2 days, and (g) 0 days prior to extreme warm event initiation. Stippled areas represent locations where the 250-hPa geopotential height anomalies are statistically distinct from climatology at the 99% confidence level. [right column] Standardized 850-hPa temperature anomalies are shaded every 0.5σ according to the legend, mean sea level pressure is contoured in black every 4 hPa, and 1000–500-hPa thickness is contoured in dashed red and blue for values greater than 540 dam and less than or equal to 540 dam, respectively, (b) 6 days, (d) 4 days, (f) 2 days, and (h) 0 days prior to extreme warm event initiation. The red ‘L’s and blue ‘H’s identify the locations of surface cyclones and anticyclones. Stippled areas represent locations where the 850-hPa temperature anomalies are statistically distinct from climatology at the 99% confidence level.